

A DUAL-SPACE MULTILEVEL KERNEL-SPLITTING FRAMEWORK FOR DISCRETE AND CONTINUOUS CONVOLUTION

SHIDONG JIANG* AND LESLIE GREENGARD†

Abstract. We introduce a new class of multilevel, adaptive, dual-space methods for computing fast convolutional transforms. These methods can be applied to a broad class of kernels, from the Green's functions for classical partial differential equations (PDEs) to power functions and radial basis functions such as those used in statistics and machine learning. The DMK (*dual-space multilevel kernel-splitting*) framework uses a hierarchy of grids, computing a smoothed interaction at the coarsest level, followed by a sequence of corrections at finer and finer scales until the problem is entirely local, at which point direct summation is applied.

Unlike earlier multilevel summation schemes, DMK exploits the fact that the interaction at each scale is diagonalized by a short Fourier transform, permitting the use of separation of variables, but without relying on the FFT. This requires careful attention to the discretization of the Fourier transform at each spatial scale. Like multilevel summation, we make use of a recursive (telescoping) decomposition of the original kernel into the sum of a smooth far-field kernel, a sequence of difference kernels, and a residual kernel, which plays a role only at leaf boxes in the adaptive tree. At all higher levels in the grid hierarchy, the interaction kernels are designed to be smooth in both physical and Fourier space, admitting efficient Fourier spectral approximations. The DMK framework substantially simplifies the algorithmic structure of the fast multipole method (FMM) and unifies the FMM, Ewald summation, and multilevel summation, achieving speeds comparable to the FFT in work per gridpoint, even in a fully adaptive context.

For continuous source distributions, the evaluation of local interactions is further accelerated by approximating the kernel at the finest level as a sum of Gaussians with a highly localized remainder. The Gaussian convolutions are calculated using tensor product transforms, and the remainder term is calculated using asymptotic methods. We illustrate the performance of DMK for both continuous and discrete sources with extensive numerical examples in two and three dimensions.

Key words. kernel split, dual space, diagonal translation, fast algorithms, multigrid, fast multipole method, prolate spheroidal wave functions, radially symmetric kernels

AMS subject classifications. 31A10, 65F30, 65E05, 65Y20

1. Introduction. Many problems in computational science involve the evaluation of discrete sums of the form

$$(1.1) \quad u_i = \sum_{j=1}^N K(\mathbf{x}_i - \mathbf{y}_j) \rho_j, \quad i = 1, \dots, N,$$

or continuous convolutions of the form

$$(1.2) \quad u(\mathbf{x}) = \int_B K(\mathbf{x} - \mathbf{y}) \rho(\mathbf{y}) d\mathbf{y},$$

where $\mathbf{x}, \mathbf{y} \in \mathbb{R}^d$ and B is a rectangular box in \mathbb{R}^d . In the present paper, we restrict our attention to kernels $K(\mathbf{x})$ which are not highly oscillatory. Examples of such kernels include many of the Green's functions governing classic partial differential equations, the Matern kernels in statistics and machine learning, the general power function $1/|\mathbf{x} - \mathbf{y}|^\alpha$, and the radial basis functions used for function approximation from point clouds of data. For both the discrete and continuous cases, we will refer to

*Center for Computational Mathematics, Flatiron Institute, Simons Foundation, New York, New York 10010 (sjiang@flatironinstitute.org)

†Center for Computational Mathematics, Flatiron Institute, Simons Foundation, New York, New York 10010 & Courant Institute of Mathematical Sciences, New York University, New York, New York 10012 (greenard@courant.nyu.edu).

ρ as the charge and to u as the potential. Since this class of problems is ubiquitous, the corresponding literature is vast. We will not attempt a comprehensive review here, but simply point out that there are, broadly speaking, two classes of fast algorithms for such problems: (a) tree-based methods such as the fast multipole method (FMM) and its variants [15, 19, 30, 34, 39, 40, 64, 77, 78] or multilevel summation [12, 13, 44, 45, 50, 57, 67], and (b) uniform grid-based methods that rely on the fast Fourier transform (FFT) such as Ewald summation (see, for example, [21, 49, 65, 66, 70]). The tree-based methods have the advantage of permitting adaptive discretization in the case of either continuous or discrete sources, and can achieve linear scaling. The FFT-based methods, on the other hand, achieve $O(N \log N)$ complexity for more or less uniform discretizations with a small constant prefactor implicit in the $O(N \log N)$ notation. They are typically preferred in applications that do not require adaptivity because of their ease of implementation and the wide availability of high-performance packages such as FFTW [31, 32]. In the discrete setting, the FFT-based methods can be understood in one of two ways: (a) mollification of the given source distribution, using the FFT to diagonalize the convolution, followed by a local correction step, or (b) splitting of the kernel $K(\boldsymbol{x})$ into a smooth far-field component and a singular near-field component (Ewald’s original approach). Both approaches can also be recast as applications of the nonuniform fast Fourier transform (NUFFT) [4, 22, 23, 38, 62]. Finally, we should also note that a “multi-level Ewald” method was proposed in [16], aimed primarily at achieving better parallel FFT performance.

The DMK method developed here draws on all of the ideas mentioned above, as well as multiresolution methods [8, 9, 10, 46]. It combines hierarchical, tree-based kernel-splitting with spatially localized Fourier transforms and leads to *adaptive* methods with $O(N)$ complexity. While it is described in detail below, we summarize the novel features that make it faster and more general than prior approaches:

1. Unlike Ewald methods, DMK *does not* depend on the FFT for its asymptotic complexity. (The lengths of the transforms used internally are independent of N , and sufficiently short that all such calculations could be carried out directly.)
2. Unlike Ewald methods, it is fully adaptive.
3. Like Ewald methods, and unlike previous multilevel summation methods, Fourier analysis is exploited to diagonalize the convolutions needed at each level.
4. Like Ewald methods, at the finest level in the adaptive tree, the interaction kernels are local and compactly supported.
5. Unlike fast multipole methods (FMMs), DMK does not separate the near and far fields, and does not rely on properties of the governing partial differential equation for compression. For readers familiar with the details of FMMs, the “interaction list” processing in DMK is much simpler - requiring only communication with near neighbors at each level in the tree hierarchy.
6. Like fast multipole methods, DMK involves a single upward pass and a single downward pass over an adaptive tree hierarchy.
7. Unlike earlier multiresolution approaches, the kernel splitting in DMK involves only a single convolution kernel at each level in the tree hierarchy.
8. Unlike earlier multilevel summation methods, DMK uses Fourier analysis to diagonalize interactions at every level.

In short, DMK blends the algorithmic structure of the FMM and multilevel methods with that of Ewald summation by combining hierarchical kernel-splitting with localized, spatially adaptive Fourier convolution. At each level, a different degree of smoothing is applied: the longest range interactions are accounted for at the coarsest levels, where the smoothing is greatest. Corrections are then computed on successively finer levels, corresponding to sharper but more localized features. Detailed Fourier analysis of these localized kernels shows that, for any fixed precision, a modest number of Fourier modes is needed at each scale, permitting an efficient, separable representation of the interaction. It is worth noting that, from the viewpoint of numerical linear algebra, the FMM and its descendants (including \mathcal{H} -matrices and skeletonization-based schemes) [30, 42, 43, 48, 56] carry out hierarchical low-rank compression *directly* on the given interaction matrix with entries $K(\mathbf{x}_i - \mathbf{y}_j)$. For singular, nonoscillatory kernels, this leads to the requirement that source and target boxes be “well-separated” in order for the sub-blocks of the interaction matrix to be sufficiently low rank. In the DMK framework (and in multilevel summation methods more generally), the interaction matrix is split into a *sum* of matrices - one for each spatial scale - that are dense (but low-rank) at coarse levels and sparse at finer levels.

We refer to DMK as a *framework* since the structure of the algorithm is largely kernel- and dimension-independent, using only generic, tensor-product Fourier convolution. The details, however, are kernel-specific, requiring some analysis in both the Fourier transform domain and physical space. Numerical experiments show that DMK leads to implementations that are as fast or faster than state-of-art codes, such as the PVFMM [53] and FMM3D [2] libraries for translation-invariant Green’s functions, and that they *retain the same speed* for more general kernels, unlike earlier FMM variants such as those in [30, 34].

The paper is organized as follows. In section 2, we summarize some of mathematical prerequisites. In section 3, we provide a detailed description of an adaptive DMK algorithm for the Poisson equation in three dimensions. In section 4, we show how to extend the DMK approach to several other kernels, and in section 5, we present the results of numerical experiments. In section 6, we discuss some potential algorithmic improvements and extensions of DMK to other problems in computational physics.

2. Mathematical preliminaries and notation. We begin by summarizing the main mathematical tools and definitions to be used throughout the paper, with some material relegated to appendix A. For a point $\mathbf{x} \in \mathbb{R}^d$, we will denote its magnitude by $r = |\mathbf{x}|$. Points in the Fourier transform domain will be denoted by \mathbf{k} with magnitude $k = |\mathbf{k}|$. When a function f is radially symmetric, we will use $f(r)$ and $f(\mathbf{x})$ interchangeably.

We will make use of multi-index notation. That is, for a d -tuple of integers (a multi-index) of the form $\mathbf{n} = (n_1, \dots, n_d)$, a point $\mathbf{x} = (x_1, \dots, x_d)$ in \mathbb{R}^d , and a scalar function of one variable $T_n(x)$, we define $T_{\mathbf{n}}(\mathbf{x}) = \prod_{i=1}^d T_{n_i}(x_i)$ and

$$\sum_{\mathbf{n} \in [1, \dots, p]^d} C_{\mathbf{n}} T_{\mathbf{n}}(\mathbf{x}) \equiv \sum_{n_1=1}^p \cdots \sum_{n_d=1}^p C_{n_1, \dots, n_d} T_{n_1-1}(x_1) \cdots T_{n_d-1}(x_d).$$

We will permit the multi-index to take on negative values. For example, we will make extensive use of formulas such as

$$\sum_{\mathbf{m} \in [-p, \dots, p]^d} w_{\mathbf{m}} e^{i\mathbf{k}_{\mathbf{m}} \cdot \mathbf{x}} \equiv \sum_{m_1=-p}^p \cdots \sum_{m_d=-p}^p w_{m_1, \dots, m_d} e^{i\mathbf{k}_{\mathbf{m}} \cdot \mathbf{x}},$$

where $\mathbf{k}_m = (k_{m_1}, \dots, k_{m_d})$.

2.1. Interpolation. Let $f(x)$ be a smooth function on the interval $[-1, 1]$. Then it is well-known to have a rapidly converging Chebyshev series [11, 72]

$$f(x) \approx \sum_{n=1}^p a_n T_{n-1}(x).$$

The Chebyshev polynomials [11, 71] can be defined by the recurrence relations

$$T_0(x) = 1, \quad T_1(x) = x, \quad T_{n+1}(x) = 2xT_n(x) - T_{n-1}(x).$$

The *Chebyshev nodes of the first kind* are the zeros of $T_p(x)$, given by

$$\{r_i = \cos \left[\frac{\pi(i - \frac{1}{2})}{p} \right], i = 1, \dots, p\}.$$

We define the $p \times p$ ‘‘Vandermonde-like’’ matrix V by $V(i, j) = T_{j-1}(r_i)$ [47] Given the vector of function values $\mathbf{f} = (f(r_1), f(r_2), \dots, f(r_p))$, the coefficients of the Chebyshev interpolant can be obtained as

$$\mathbf{a} = V^{-1} \mathbf{f},$$

where $\mathbf{a} = (a_1, \dots, a_p)$.

Given a set of N additional points $\{-1 \leq \xi_k \leq 1 \mid k = 1, \dots, N\}$, we define the $N \times p$ *evaluation matrix* E by $E(k, n) = T_{n-1}(\xi_k)$, so that $E \mathbf{a}$ is the value of the interpolant at the additional points. The mapping from function values at the Chebyshev nodes $\{r_j\}$ to function values at the additional points $\{\xi_k\}$ is clearly given by the *interpolation matrix* $U = E V^{-1} \in \mathbb{R}^{N \times p}$.

In d dimensions, we denote by $\{\mathbf{r}_i\}$ the tensor product Chebyshev nodes. That is, $\mathbf{r}_i = (r_{i_1}, \dots, r_{i_d})$ for the multi-index \mathbf{i} . We will continue to denote the corresponding $p^d \times p^d$ matrix by V and write $V(\mathbf{i}, \mathbf{j}) = T_{j-1}(\mathbf{r}_i)$ for Chebyshev interpolation. Here, the multi-index $\mathbf{j} - \mathbf{1} = (j_1 - 1, \dots, j_d - 1)$. Given the function values $\mathbf{f} = f(\mathbf{r}_j)$ for $\mathbf{j} \in [1, \dots, p]^d$, the coefficients of the Chebyshev interpolant are given by

$$\mathbf{a} = V^{-1} \mathbf{f}$$

where we are omitting the details of ‘‘unrolling’’ the multi-indices and $\mathbf{a} = \{a_{\mathbf{i}} \mid \mathbf{i} \in [1, \dots, p]^d\}$. For N additional points $\{\boldsymbol{\xi}_k \in [-1, 1]^d \mid k = 1, \dots, N\}$, the $N \times p^d$ evaluation matrix E is given by $E(k, \mathbf{n}) = T_{\mathbf{n}-\mathbf{1}}(\boldsymbol{\xi}_k)$ and the interpolation matrix by $U = E V^{-1} \in \mathbb{R}^{N \times p^d}$.

If the targets themselves lie on a tensor product grid with multi-index \mathbf{q} , we will write $E(\mathbf{q}, \mathbf{n})$ for the corresponding $q^d \times p^d$ evaluation matrix. The interpolation matrix is again defined by

$$(2.1) \quad U = E V^{-1} \in \mathbb{R}^{q^d \times p^d}.$$

2.2. Anterpolation. Suppose now that, in one dimension, we have a potential function expressed in terms of some smooth kernel $K(x)$ of the form

$$(2.2) \quad u(x) = \sum_{j=1}^N \rho_j K(x - x_j),$$

with $x_j \in [-1, 1]$. It is convenient to adopt the language of electrostatics, and we will refer to ρ_j as a *charge* located at x_j . Since $K(x)$ is a smooth function, viewing x as fixed, we may write

$$(2.3) \quad u(x) \approx \sum_{j=1}^N \rho_j \left[\sum_{i=1}^p K(x - r_i) U(j, i) \right],$$

where U is the interpolation matrix mapping from the Chebyshev nodes $\{r_i\}$ to the points $\{x_j\}$. Changing the order of summation, we may write

$$(2.4) \quad u(x) \approx \sum_{i=1}^p \tilde{\rho}_i K(x - r_i),$$

with

$$(2.5) \quad \tilde{\rho}_i = \sum_{j=1}^N U^T(i, j) \rho_j.$$

DEFINITION 2.1. *The transpose of the interpolation matrix, $U^T = V^{-T} E^T$ is generally referred to as the “anterpolation” matrix. The charges $\{\tilde{\rho}_j\}$ defined in (2.5) will be referred to as “proxy” charges. In higher dimensions, proxy charges are defined in the same way. That is, for a smooth potential function such as*

$$(2.6) \quad u(\mathbf{x}) = \sum_{j=1}^N \rho_j K(\mathbf{x} - \mathbf{x}_j),$$

we have

$$(2.7) \quad u(\mathbf{x}) \approx \sum_{\mathbf{i} \in [1, \dots, p]^d} \tilde{\rho}_{\mathbf{i}} K(\mathbf{x} - \mathbf{r}_{\mathbf{i}}),$$

where

$$(2.8) \quad \tilde{\rho}_{\mathbf{i}} = \sum_{j=1}^N U^T(\mathbf{i}, j) \rho_j.$$

Anterpolation is a key step in accelerating the “fine-to-coarse” transition in a variety of tree-based methods [12, 13, 67, 44, 45, 50, 57] and, in d dimensions, the cost of computing (2.8) is clearly $O(Np^d)$. If the sources ρ_j in (2.6) lie on a tensor-product grid, however, that cost can be reduced.

LEMMA 2.2. *Suppose that the charges ρ_j in (2.6) lie on a tensor product Chebyshev grid contained within $[-1, 1]^d$. Then the mapping*

$$(2.9) \quad \tilde{\rho}_{\mathbf{i}} = \sum_{j \in [1, \dots, p]^d} U^T(\mathbf{i}, j) \rho_j$$

can be computed in $O(p^{d+1})$ operations, where U is defined in (2.1).

The proof follows from a straightforward application of separation of variables, since the Chebyshev nodes $\{\mathbf{r}_{\mathbf{i}}\}$ are themselves on a tensor product grid. (Lemma 2.2

is used in [subsection 3.3](#) below to merge the proxy charges from child boxes to a smaller set of proxy charges for their parent.)

Given a smooth function on the box $B = [-1, 1]^d$, we will also need to shift the corresponding Chebyshev expansion to a box C of width 1 centered at $\mathbf{c} = (\pm\frac{1}{2}, \dots, \pm\frac{1}{2})$. (In the context of hierarchical tree-based solvers, one can think of B as a parent box and C as one of its 2^d children.)

LEMMA 2.3. *Suppose that we are given a tensor-product polynomial on a box B of the form*

$$u(\mathbf{x}) = \sum_{\mathbf{n} \in [1, \dots, p]^d} \alpha_{\mathbf{n}} T_{\mathbf{n}-1}(\mathbf{x}),$$

where the Chebyshev polynomials are centered at the center of B and scaled to the box size. Then, in a child box $C \subset B$,

$$u(\mathbf{x}) = \sum_{\mathbf{n}' \in [1, \dots, p]^d} \beta_{\mathbf{n}'} T'_{\mathbf{n}'-1}(\mathbf{x}),$$

where the Chebyshev polynomials $T'_{\mathbf{n}'-1}(\mathbf{x})$ are centered on C and scaled to its size. This translation is exact and

$$(2.10) \quad \beta_{\mathbf{n}'} = V^{-1} E \alpha_{\mathbf{n}}$$

where $E(\mathbf{k}, \mathbf{n}) = T_{\mathbf{n}-1}(\mathbf{r}'_{\mathbf{k}})$ is the evaluation matrix entry for scaled Chebyshev node $\mathbf{r}'_{\mathbf{k}}$ on C and V is the (multi-index) Vandermonde matrix. The mapping in (2.10) can be computed in $O(p^{d+1})$ operations.

The exactness of the translation is obvious since we are simply shifting the center of a polynomial in d variables. The reduction in computational cost from the naive estimate $O(p^{2d})$ to $O(p^{d+1})$ follows from separation of variables.

REMARK 2.4. *The order of polynomial approximation to be used depends on the desired precision of the calculation and the smoothness of the kernel in (2.6). Using Chebyshev interpolation, we have the standard error estimate [63, 72]*

$$|f(x) - P_{n-1}(x)| \leq \frac{1}{2^n n!} \left(\frac{b-a}{2} \right)^n \|f^{(n)}\|_{\infty}.$$

Below, we will focus on the systematic use of band-limited (or approximately band-limited) functions, whose Fourier transform is supported in $[-K_{\max}, K_{\max}]$, which satisfy

$$\|f^{(n)}\|_{\infty} \leq K_{\max}^n \|f\|_{\infty}.$$

If the approximation is used on an interval of size $1/K_{\max}$, then clearly

$$|f(x) - P_{n-1}(x)| = O\left(\frac{1}{2^n n!}\right) \|f\|_{\infty},$$

indicating rapid convergence with n , and independent of K_{\max} .

2.3. The Fourier transform and its properties. We define the Fourier transform of F by

$$(2.11) \quad \widehat{F}(\mathbf{k}) = \int e^{-i\mathbf{k} \cdot \mathbf{x}} F(\mathbf{x}) d\mathbf{x},$$

for $\mathbf{x}, \mathbf{k} \in \mathbb{R}^d$. The function $F(\mathbf{x})$ can be recovered from the inverse transform

$$(2.12) \quad F(\mathbf{x}) = \frac{1}{(2\pi)^d} \int e^{i\mathbf{k}\cdot\mathbf{x}} \widehat{F}(\mathbf{k}) d\mathbf{k}.$$

Some well-known properties of the Fourier transform are [24, 71]:

- (a) If $c \in \mathbb{R}$ with $c \neq 0$, then $\mathcal{F}\{f(\frac{\mathbf{x}}{c})\}(\mathbf{k}) = |c|^d \widehat{f}(|c|\mathbf{k})$. (Dilation)
- (b) $\mathcal{F}\{\Delta^\alpha f(\mathbf{x})\}(\mathbf{k}) = -|\mathbf{k}|^{2\alpha} \widehat{f}(\mathbf{k})$. (Differentiation)
- (c) $f(\mathbf{x})$ is smooth if and only if $\widehat{f}(\mathbf{k})$ decays rapidly as $k \rightarrow \infty$. (Duality)
- (d) The Poisson summation formula [24] states that

$$(2.13) \quad \sum_{n=-\infty}^{\infty} f\left(x + \frac{2\pi n}{h}\right) = \frac{h}{2\pi} \sum_{m=-\infty}^{\infty} \widehat{f}(mh) e^{imhx}.$$

This holds for a broad class of functions, and extends to distributions such as the Dirac delta function.

3. DMK for the 3D Laplace kernel. In this section, we consider the free-space Green's function for the Laplace equation in three dimensions, and begin with a review of how classical (single level) Ewald summation [49, 21, 65]) can be applied to the calculation of the discrete sum

$$(3.1) \quad u_i = \sum_{j=1}^N \frac{1}{|\mathbf{x}_i - \mathbf{y}_j|} \rho_j, \quad i = 1, \dots, N,$$

where (for the moment) we assume the targets $\{\mathbf{x}_i\}$ are disjoint from the sources $\{\mathbf{y}_j\}$. We then show how to create, using multilevel kernel-splitting, a fast and fully adaptive variant of the method with $O(N \log N)$ complexity. Simple modifications of the method yield an even more efficient $O(N)$ method. In subsection 3.6, we show that significant acceleration can be obtained for continuous sources at the level of leaf boxes by approximating the kernel using a sum-of-Gaussians combined with asymptotic analysis. Finally, in subsection 3.7, we show that a further reduction in cost can be achieved using prolate spheroidal wave functions in the kernel-splitting framework.

3.1. Classical Ewald summation. In order to reduce the cost of the calculation (3.1), Ewald [27] began by rewriting the 3D Laplace kernel in the form

$$(3.2) \quad \frac{1}{r} = M(r) + R(r) := \frac{\operatorname{erf}(r/\sigma)}{r} + \frac{\operatorname{erfc}(r/\sigma)}{r},$$

where erf and erfc are the error and complementary error functions

$$(3.3) \quad \operatorname{erf}(x) = \frac{2}{\sqrt{\pi}} \int_0^x e^{-t^2} dt, \quad \operatorname{erfc}(x) = 1 - \operatorname{erf}(x),$$

and σ is a free parameter, to be chosen for optimal performance later. Note that, once $r \geq 6\sigma$, $\operatorname{erf}(r/\sigma) \approx 1$ with more than fifteen digits of accuracy and $\operatorname{erfc}(r/\sigma) \approx 0$. Thus, $M(r)$ accurately represents the $\frac{1}{r}$ potential in the far field and $R(r)$ can be viewed as a local correction that needs to be invoked for $r < 6\sigma$. Note also that the mollified far-field kernel $M(r)$ is smooth but slowly decaying, while the residual kernel $R(r)$ is singular but compactly supported (to a fixed precision). The smoothness of

$M(r)$ follows from the fact that the Taylor series of the error function $\text{erf}(r)$ about the origin contains only odd powers of r .

Combining (3.2) and (3.1), we may write

$$(3.4) \quad u_i = u_i^{\text{far}} + u_i^{\text{local}}$$

where

$$u_i^{\text{far}} = \sum_{j=1}^N M(|\mathbf{x}_i - \mathbf{y}_j|) \rho_j, \quad u_i^{\text{local}} = \sum_{j=1}^N R(|\mathbf{x}_i - \mathbf{y}_j|) \rho_j.$$

REMARK 3.1. *To evaluate the field at one of the source locations, say \mathbf{y}_i , it is physically sensible to set the “self-interaction” to zero. For this, we may write*

$$(3.5) \quad \begin{aligned} u(\mathbf{y}_i) &= u_i^{\text{self}} + u_i^{\text{far}} + u_i^{\text{local}} \\ &:= -\frac{2}{\sqrt{\pi}\sigma} \rho_i + \sum_{j=1}^N M(|\mathbf{y}_i - \mathbf{y}_j|) \rho_j + \sum_{\substack{j=1 \\ j \neq i}}^N R(|\mathbf{y}_i - \mathbf{y}_j|) \rho_j. \end{aligned}$$

The first term is a “self-interaction” correction, needed to account for the fact that, in the smoothed far field sum,

$$(3.6) \quad \lim_{r \rightarrow 0} M(r) = \frac{2}{\sqrt{\pi}\sigma}.$$

The far field contribution is amenable to Fourier-based methods. It is straightforward to check that the Fourier transform of the mollified far-field kernel $M(|\mathbf{x}|)$ is given by

$$(3.7) \quad \widehat{M}(\mathbf{k}) = 4\pi \frac{e^{-k^2 \sigma^2 / 4}}{k^2},$$

for $\mathbf{k} \in \mathbb{R}^3$, where $k = |\mathbf{k}|$. It decays rapidly, but is singular at $k = 0$.

REMARK 3.2. *In its original form, Ewald summation was developed for problems with periodic boundary conditions [21, 27, 49]. In that setting, the far field contribution is expressed as a rapidly converging Fourier series, avoiding the Fourier transform along with issues of quadrature in the Fourier domain. The singularity of $\widehat{F}(\mathbf{k})$ at the origin is ignored, because of the requirement of charge neutrality in the unit box for periodic problems. In recent years, however, Ewald methods have been extended to address problems with either periodic or free-space boundary conditions in any coordinate direction. See [3, 1, 65] for a detailed discussion.*

In this paper, we restrict our attention to the free-space problem and modify the original Ewald method accordingly, assuming only that the point locations $\{\mathbf{x}_i, \mathbf{y}_i \mid i = 1, \dots, N\}$ have been rescaled and centered so that they lie in the unit box $[-1/2, 1/2]^d$.

Since we will compute the far field interactions via the Fourier transform, it is convenient to replace the kernel $M(|\mathbf{x}|)$ with a *windowed* kernel, which we define as

$$(3.8) \quad W(\mathbf{x}) = \frac{1}{(2\pi)^3} \int_{\mathbf{k} \in \mathbb{R}^3} e^{i\mathbf{k} \cdot \mathbf{x}} \widehat{W}(\mathbf{k}) d\mathbf{k},$$

where

$$(3.9) \quad \widehat{W}(\mathbf{k}) = 8\pi \left(\frac{\sin(\tilde{C}|\mathbf{k}|/2)}{|\mathbf{k}|} \right)^2 e^{-|\mathbf{k}|^2 \sigma^2 / 4},$$

a C^∞ function, depending on a parameter \tilde{C} . This makes discretization very simple, since the integrand in (3.8) is smooth and exponentially decaying, so that the tensor product trapezoidal rule yields spectral accuracy (see, for example, [73]). It is only permissible to do this, of course, if the substitution of $W(\mathbf{x})$ for $M(\mathbf{x})$ yields the same result, as established in Lemma 3.4.

REMARK 3.3. *The elimination of the singularity in $\widehat{M}(\mathbf{k})$ at the origin in (3.7) by applying a sharp window in physical space was developed systematically in [74], where it was applied to a variety of constant coefficient PDEs with smooth, compactly supported right-hand sides. The basic observation (for the Laplace kernel) is that the kernel $1/r$ truncated at a distance \tilde{C} has the smooth Fourier transform*

$$8\pi \left(\frac{\sin(\tilde{C}|\mathbf{k}|/2)}{|\mathbf{k}|} \right)^2.$$

Here, we apply this approach to the mollified kernel $M(|\mathbf{x}|)$.

LEMMA 3.4. *Let $C = \sqrt{3}$, the diameter of the unit box in three dimensions, and let the parameter defining \widehat{W} in (3.9) be given by $\tilde{C} = C + b\sigma$. Then, for sources and targets in the unit box $[-1/2, 1/2]^3$, we have*

$$(3.10) \quad u_i^{\text{far}} = \sum_{j=1}^N M(|\mathbf{x}_i - \mathbf{y}_j|) \rho_j \approx \sum_{j=1}^N W(\mathbf{x}_i - \mathbf{y}_j) \rho_j,$$

with a relative error of the order $\text{erfc}(b)$. (Setting $b = 6$ yields better than fifteen digits of accuracy.)

Proof. From (3.9) and the duality property in subsection 2.3, we know that the kernel $W(\mathbf{x}) = W(|\mathbf{x}|)$ is a smooth radial function. We now show that it is given explicitly by

$$(3.11) \quad W(r) = \frac{\text{erf}(r/\sigma)}{r} - \frac{1}{2} \left(\frac{\text{erf}((b\sigma + C + r)/\sigma)}{r} - \frac{\text{erf}((b\sigma + C - r)/\sigma)}{r} \right).$$

For this, we combine (2.12) and (A.6) to obtain the Fourier transform relation

$$(3.12) \quad F(r) = \frac{1}{2\pi^2} \int_0^\infty \frac{\sin(kr)}{kr} \hat{F}(k) k^2 dk$$

for any radially symmetric function F . Thus,

$$\begin{aligned} W(r) &= \frac{1}{2\pi^2} \int_0^\infty \frac{\sin(kr)}{kr} \hat{W}(k) k^2 dk \\ &= \frac{4}{\pi} \int_0^\infty \frac{\sin(kr)}{kr} \sin^2((b\sigma + C)k/2) e^{-k^2\sigma^2/4} dk \\ &= \frac{2}{\pi} \int_0^\infty \frac{\sin(kr)}{kr} (1 - \cos(k(b\sigma + C))) e^{-k^2\sigma^2/4} dk \\ &= \frac{2}{\pi} \int_0^\infty \frac{e^{-k^2\sigma^2/4}}{kr} (\sin(kr) - \frac{1}{2} \sin(k(b\sigma + C + r)) + \frac{1}{2} \sin(k(b\sigma + C - r))) dk. \end{aligned}$$

Applying (3.12) to the mollified kernel $M(r)$, and using (3.7), it is straightforward to see that

$$(3.13) \quad \text{erf}(r/\sigma) = \frac{2}{\pi} \int_0^\infty \frac{e^{-k^2\sigma^2/4}}{k} \sin(kr) dk,$$

and the result (3.11) follows. Combining (3.2) and (3.11), we have

$$(3.14) \quad |W(r) - M(r)| = \frac{\operatorname{erf}((b\sigma + C + r)/\sigma) - \operatorname{erf}((b\sigma + C - r)/\sigma)}{2r} \\ \leq \operatorname{erfc}(b) \frac{1}{r}, \quad r \leq C,$$

as desired. \square

Although we have an explicit expression for $W(\mathbf{x})$, the calculation of (3.10) is most rapidly carried out using Fourier convolution. Given $\sigma > 0$ and $\epsilon < 1$, assuming

$$(3.15) \quad K_{\max}^2 \sigma^2 / 4 \geq \log(1/\epsilon),$$

we have

$$(3.16) \quad u_i^{\text{far}} = \frac{1}{(2\pi)^3} \int_{-K_{\max}}^{K_{\max}} e^{i\mathbf{k} \cdot \mathbf{x}_i} \widehat{W}(\mathbf{k}) \widehat{g}(\mathbf{k}) d\mathbf{k} + O(\epsilon),$$

where

$$(3.17) \quad \widehat{g}(\mathbf{k}) = \sum_{j=1}^N e^{-i\mathbf{k} \cdot \mathbf{y}_j} \rho_j.$$

It is easy to see that the number of oscillations of the integrand in each dimension is at most $O((C + \tilde{C})K_{\max}/(2\pi)) = O(\sqrt{\log(1/\epsilon)}/\sigma)$. Thus, once the total number of quadrature nodes $N_F = (2n + 1)^3$, with $n \approx K_{\max}$ (Nyquist sampling), the error in

$$(3.18) \quad u_i^{\text{far}} \approx \sum_{\mathbf{m} \in [-n, \dots, n]^d} \frac{1}{\pi^2} \left(\frac{\sin(\tilde{C}|\mathbf{k}_{\mathbf{m}}|/2)}{|\mathbf{k}_{\mathbf{m}}|} \right)^2 e^{-|\mathbf{k}_{\mathbf{m}}|^2 \sigma^2 / 4} e^{i\mathbf{k}_{\mathbf{m}} \cdot \mathbf{x}_i} \widehat{g}(\mathbf{k}_{\mathbf{m}})$$

decays superalgebraically. Here, $\mathbf{k}_{\mathbf{m}} = \frac{K_{\max}}{n} \mathbf{m} = \frac{K_{\max}}{n} (m_1, m_2, m_3)$.

It is convenient to write the far field contribution in the form

$$(3.19) \quad u_i^{\text{far}} = \sum_{\mathbf{m} \in [-n, \dots, n]^d} w_{\mathbf{m}} e^{i\mathbf{k}_{\mathbf{m}} \cdot \mathbf{x}_i} \widehat{g}(\mathbf{k}_{\mathbf{m}}), \quad i = 1, \dots, N,$$

where

$$(3.20) \quad w_{\mathbf{m}} = \frac{1}{\pi^2} \left(\frac{\sin(\tilde{C}|\mathbf{k}_{\mathbf{m}}|/2)}{|\mathbf{k}_{\mathbf{m}}|} \right)^2 e^{-|\mathbf{k}_{\mathbf{m}}|^2 \sigma^2 / 4}.$$

We may rewrite (3.19) more explicitly in terms of matrix-vector products as follows (omitting the details of unrolling the multi-index \mathbf{m} to a single index m that ranges from 1 to N_F):

$$(3.21) \quad u^{\text{far}} = \mathcal{F}_2 \mathcal{D} \mathcal{F}_1 \rho,$$

where

$$(3.22) \quad u^{\text{far}} = [u_1^{\text{far}} \dots u_N^{\text{far}}]^T, \quad \rho = [\rho_1 \dots \rho_N]^T,$$

\mathcal{F}_1 is an $N_F \times N$ matrix with entries $\mathcal{F}_1(m, j) = e^{-i\mathbf{k}_m \cdot \mathbf{y}_j}$, \mathcal{D} is an $N_F \times N_F$ diagonal matrix with entries $\mathcal{D}(m, m) = w_m$, and \mathcal{F}_2 is an $N \times N_F$ matrix with entries $\mathcal{F}_2(i, m) = e^{i\mathbf{k}_m \cdot \mathbf{x}_i}$.

The application of \mathcal{F}_1 or \mathcal{F}_2 to a vector requires only $O(N_F \log N_F + N \log^3(1/\epsilon))$ work using the type-1 and type-2 nonuniform fast Fourier transform (NUFFT) [4, 6, 22, 23, 38, 62], where ϵ is the desired precision. The application of \mathcal{D} clearly requires $O(N_F)$ work.

Let us now assume that we have divided the computational domain into a grid with $N_B = 8^L$ cells (boxes), each of side length $r_L = 2^{-L}$. (In d dimensions, there are 2^{dL} boxes after L levels of uniform refinement, with each refinement by a factor of 2.) Assuming that the particles are uniformly distributed, the number of particles in each box is approximately the average value $n_s = N/(8^L)$.

We now choose σ so that, when computing the local part,

$$u_i^{\text{local}} = \sum_{j=1}^N R(|\mathbf{x}_i - \mathbf{y}_j|) \rho_j$$

for a target \mathbf{x}_i in a box B with side length r_L , the interactions are negligible beyond the 3^3 nearest neighbors in the uniform grid, including itself. That is to say, we would like to enforce that $\text{erfc}(r/\sigma) \leq \epsilon$ for $r \geq r_L$. A sufficient condition is that

$$(3.23) \quad \sigma \approx \frac{r_L}{\sqrt{\log(1/\epsilon)}}.$$

From the discussion above, the number of Fourier modes needed for the far field computation is

$$(3.24) \quad N_F = O(K_{\text{max}}^3) = O\left(\left(\frac{\log(1/\epsilon)}{r_L}\right)^3\right) = O\left(\frac{N}{n_s} \log^3(1/\epsilon)\right).$$

With this choice of σ , the cost of evaluating all local interactions is bounded by $3^3 n_s N$ evaluations of the residual kernel $R(|\mathbf{x}_i - \mathbf{y}_j|)$. In summary, the local interactions require of the order $O(N n_s)$ work and the far field interactions require of the order $O(N \log \frac{N}{n_s})$ work. For $n_s = O(1)$, this leads to an $O(N \log N)$ method. The optimal choice of n_s , of course, is the value that balances the far field and local work, which depends on the precision ϵ , the precise value of N_F and the cost of residual kernel evaluations. Finally, we should note that we have used a grid with 8^L boxes for convenience only; any uniform grid on which the FFT is efficient can be used.

3.2. An $O(N \log N)$ DMK method. We turn now to the development of an adaptive, hierarchical extension of Ewald's method, which will also require $O(N \log N)$ work, but does not rely on the FFT for its asymptotic complexity. Recall that the problem with highly nonuniform particle distributions is that we cannot bound the number of particles that lie in any single box B in a uniform grid with $O(N)$ boxes. As a result, we cannot control the cost of the local interactions. Creating a uniform grid with smaller boxes would require that $N_F \gg N$, increasing the cost of the far-field interactions. Thus, an adaptive data structure is essential, and we shall rely here on a level-restricted oct-tree in three dimensions (and on a level-restricted quad-tree in two dimensions) [69]. The tree construction begins with the unit box in dimension d and sorts all sources and targets into its 2^d children, obtained by bisecting the box in each coordinate direction. The refinement process is continued

recursively until there are fewer than n_s sources and targets in any leaf node, with the usual convention of referring to the box that is subdivided as the *parent* and the 2^d subdivisions as its children. The free parameter n_s is typically chosen in a precision-dependent manner, discussed in more detail below. The requirement of level-restriction is that no two boxes that share a boundary point in the data structure can be more than one refinement level apart, and there are standard algorithms to enforce such a condition [69]. In a level-restricted tree, for any box B at level l , we will refer to the boxes at the same refinement level which share a boundary point as *colleagues*, including B itself. Boxes which share a boundary point with box B at level l but are themselves leaf nodes at level $l - 1$ will be referred to as *coarse neighbors* (see Figure 3.1). The set of coarse neighbors will be denoted by $\mathcal{N}(B)$. We will refer to the unit box itself as level 0 and to the maximum refinement level as L_{\max} . The linear dimension of a box at level l will be denoted by $r_l = 2^{-l}$.

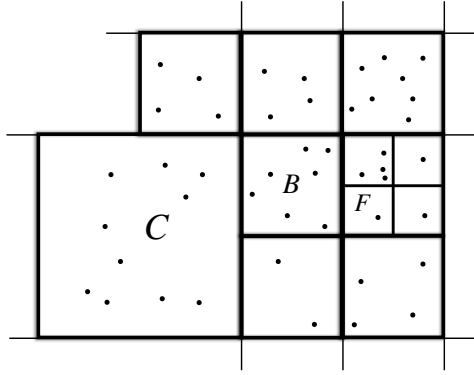


Fig. 3.1: A portion of a level-restricted tree is depicted (in two dimensions). For a leaf node B , the boxes at the same level are called *colleagues*, while F is a fine neighbor and C is a coarse neighbor.

Let us now consider the following “telescoping” decomposition of the Laplace kernel for each level $L \in \{0, \dots, L_{\max}\}$:

$$(3.25) \quad \frac{1}{r} = W_0(r) + \sum_{l=0}^{L-1} D_l(r) + R_L(r), \quad L = 0, \dots, L_{\max},$$

where the windowed kernel W_0 , the difference kernels D_l , and the residual kernels R_L are defined by the formulas

$$(3.26) \quad \begin{aligned} W_0(r) &\approx M_0(r) = \frac{\operatorname{erf}(r/\sigma_0)}{r}, \\ D_l(r) &= \frac{\operatorname{erf}(r/\sigma_{l+1}) - \operatorname{erf}(r/\sigma_l)}{r}, \\ R_L(r) &= \frac{\operatorname{erfc}(r/\sigma_L)}{r}, \end{aligned}$$

for $\sigma_0 > \sigma_1 > \dots > \sigma_{L_{\max}}$. It is easy to see that (3.25) is indeed an equality at every

level $L = 0, \dots, L_{\max}$. We define the mollified far-field kernel at level $L \geq 1$ by

$$(3.27) \quad M_L(r) = \frac{\operatorname{erf}(r/\sigma_L)}{r} = M_0(r) + \sum_{l=0}^{L-1} D_l(|\mathbf{x}|).$$

Far field interactions beyond the colleagues at level L are accounted for in terms of the kernel $M_L(|\mathbf{x}|)$ to the desired precision, and the remaining corrections involve the residual kernel $R_L(|\mathbf{x}|)$ only within colleagues and coarse neighbors. (At level $L = 1$, of course, the colleagues cover the entire computational domain.)

The departure from the classical Ewald approach (3.2), is the telescoping decomposition of the free-space Green's function and the introduction of the more and more localized difference kernels D_l as we proceed from level to level in a tree hierarchy (hence the nomenclature “kernel-splitting”). Unlike previous multilevel summation methods [12, 13, 67, 44, 45, 50, 57], we systematically rely on Fourier analysis to compute convolutions at each scale. As for the values of σ_l ($l = 0, \dots, L_{\max}$), they are chosen so that at every scale, the residual kernel R_l is supported within nearest neighbors at the same level. That is, we require that $\operatorname{erfc}(r/\sigma_l) \leq \epsilon$ for $r \geq r_l = 2^{-l}$. This is accomplished by letting

$$(3.28) \quad \sigma_0 \approx \frac{r_0}{\sqrt{\log(1/\epsilon)}}, \quad \sigma_l = \sigma_{l-1}/2.$$

The full $O(N \log N)$ scheme is illustrated in Figure 3.2. Before presenting the algorithm in detail, several observations are in order.

- (a). The windowed kernel $W_0(\mathbf{x})$ has the same behavior as in the classical Ewald approach, with a smooth and rapidly decaying Fourier transform. Here, however, σ_0 is so large that the number of quadrature nodes N_F in the Fourier transform is independent of N (the number of particles) and is simply a function of the precision with

$$N_F \approx (4 \log(1/\epsilon))^d$$

from (3.15).

- (b). For a particle in a box B at level l , the difference kernel $D_l(\mathbf{x}) = D_l(|\mathbf{x}|)$ is negligible (smaller than the requested precision ϵ) beyond B 's colleagues. It is a smooth function of $\mathbf{x} \in \mathbb{R}^3$ and its Fourier transform is given by the formula

$$(3.29) \quad \hat{D}_l(\mathbf{k}) = \begin{cases} 4\pi \frac{e^{-|\mathbf{k}|^2 \sigma_{l+1}^2/4} - e^{-|\mathbf{k}|^2 \sigma_l^2/4}}{|\mathbf{k}|^2}, & \mathbf{k} \neq (0, 0, 0) \\ \pi(\sigma_l^2 - \sigma_{l+1}^2), & \mathbf{k} = (0, 0, 0) \end{cases}$$

As above, the combination of smoothness and rapid decay implies that the trapezoidal-rule approximation to the Fourier integral converges at an exponentially rate.

- (c). When proceeding from level l to level $l + 1$, σ decreases by a factor of two, according to (3.28), so that the range of integration in the corresponding Fourier integral doubles, with

$$(3.30) \quad K_l \approx \frac{4}{r_l} \log \left(\frac{1}{\epsilon} \right)$$

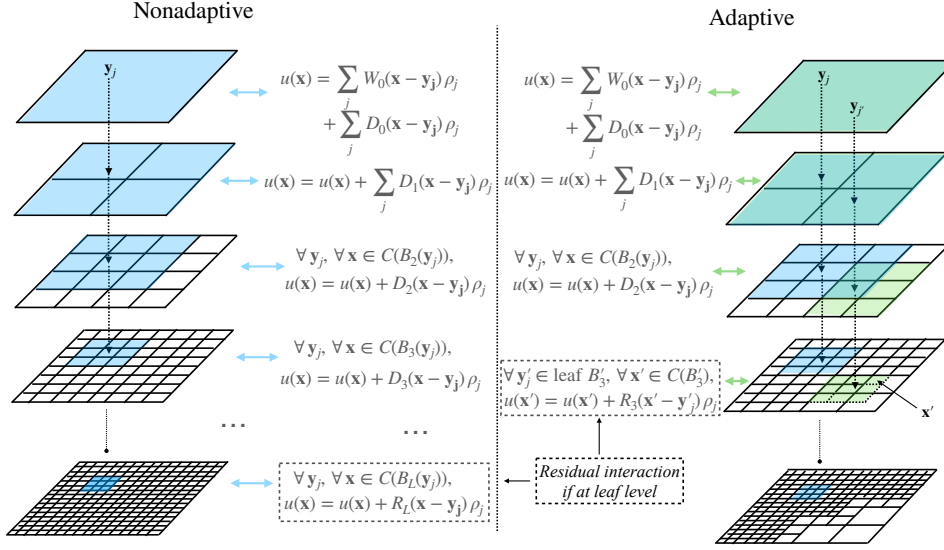


Fig. 3.2: The introduction of the telescoping series (3.25) allows for a multi-level version of Ewald summation, illustrated in two dimensions. Convolution at level 0 with W_0 is global, but requires only a short Fourier transform, whose length is independent of the number of particles. At successively finer levels, convolution with the difference kernels D_l is carried out for colleagues (nearest neighbors) only. In the nonadaptive case (left), each source \mathbf{y}_j lies in some leaf box B at the finest level, and direct interactions are computed with the residual kernel R_L for targets within B 's colleagues. In the adaptive case (right), some sources such as \mathbf{y}' may lie in a leaf box at some coarser level l (here, $l = 3$). That leaf box is denoted by B_3' in the figure. Direct interactions are computed using the residual kernel R_3 for the targets within B_3' and its colleagues. Aside from some care in bookkeeping, implementation of the adaptive scheme is straightforward.

to maintain the same level of accuracy. However, the distance between relevant sources and targets shrinks by a factor of two at the same time, so that the number of oscillations, and the number of quadrature nodes in the range $[-K_l, K_l]^d$, remains constant. (K_l can actually be set slightly smaller than the value in (3.30) because of the extra factor $1/|\mathbf{k}|^2$ in (3.29).)

- (d). In the multilevel DMK algorithm, we use localized Fourier convolution to compute the influence of the difference kernels due to sources that lie within every box B at level l with targets that lie within B or its colleagues. As a result, our trapezoidal quadrature must be accurate in a ball of radius $2r_l = r_{l-1}$. From the Poisson summation formula (2.13), it can be shown [73] that

$$(3.31) \quad \frac{2\pi}{h_l} \geq \frac{3}{2}r_l \Rightarrow h_l \leq \frac{4\pi}{3r_l}$$

is sufficient to achieve a precision ϵ for $|\mathbf{x}| \leq 2r_l$, so that we have

$$(3.32) \quad D_l(\mathbf{x}) \approx \frac{1}{(2\pi)^3} \sum_{\mathbf{k} \in [-n_f, \dots, n_f]^d} e^{i h_l \mathbf{k} \cdot \mathbf{x}} \hat{D}_l(h_l \mathbf{k}),$$

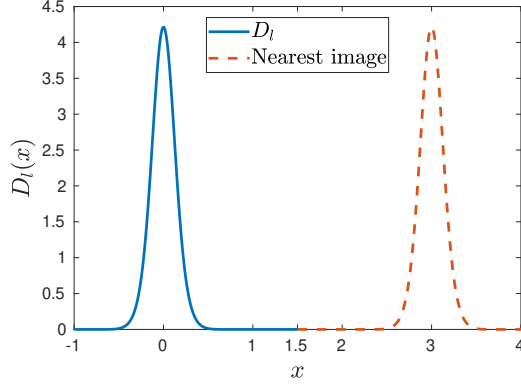


Fig. 3.3: The difference kernel D_l is compactly supported on a ball of radius r_l ($= 1$ in the figure) to the desired precision, while its Fourier spectral approximation needs to be valid on a ball of radius $2r_l$. Since the actual support of D_l is smaller than the full interval, its periodic images only need to be $\frac{3}{2}r_l$ away in order to avoid the aliasing error which controls the accuracy of its Fourier spectral approximation. This accounts for the factor of $\frac{3}{2}$ in (3.31).

where

$$(3.33) \quad n_f = \frac{K_l}{h_l} = \frac{3}{\pi} \log \left(\frac{1}{\epsilon} \right).$$

(Similar, but less sharp, estimates can be derived from the Euler-Maclaurin formula.) Using the same notation as for the classical Ewald approach, we will write

$$(3.34) \quad D_l(\mathbf{x}) \approx \sum_{\mathbf{m} \in [-n_f, \dots, n_f]^d} w_{l, \mathbf{m}} e^{i\mathbf{k}_m \cdot \mathbf{x}},$$

where $\mathbf{k}_m = h_l(m_1, m_2, m_3)$ and

$$(3.35) \quad w_{l, \mathbf{m}} = \frac{1}{(2\pi)^3} \hat{D}_l(\mathbf{k}_m).$$

The total number of Fourier modes needed for the difference kernels is

$$(3.36) \quad N_F = (2n_f + 1)^3 \approx \left(\frac{6}{\pi} \log \left(\frac{1}{\epsilon} \right) \right)^3,$$

independent of the level.

- (e). The residual kernel at level L , $R_L(|\mathbf{x}|)$, is compactly supported to precision ϵ within a ball of radius r_L , the boxsize at level L .

Suppose now that the target point \mathbf{x}_i (not coincident with any source) lies in some leaf box B_L at level L , with $B_L \subset B_{L-1} \dots \subset B_0$ denoting the hierarchy of parents at

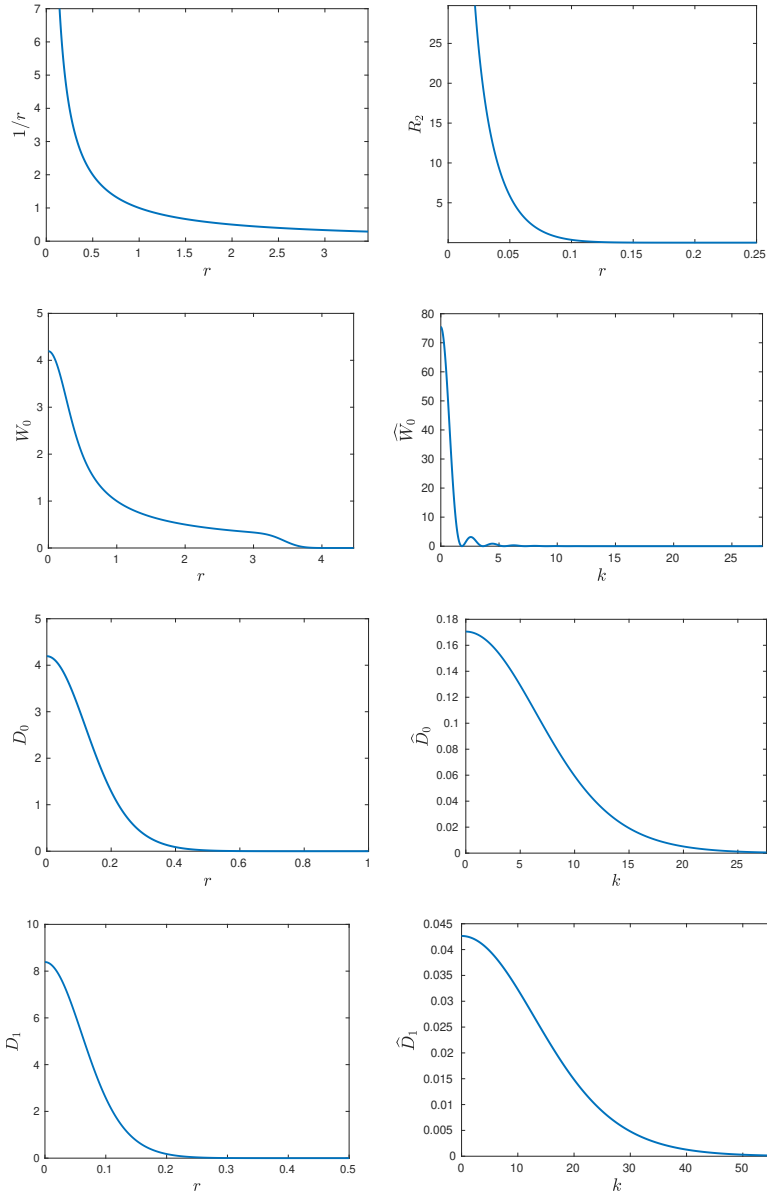


Fig. 3.4: The dual-space splitting of the $1/r$ kernel using Gaussians on a leaf box at level 2 with six digits of accuracy: $1/r = W_0(r) + D_0(r) + D_1(r) + R_2(r)$ for $r \leq \sqrt{3}$. Top row: left - the original kernel $1/r$; right - the residual kernel $R_2(r)$ that is numerically supported on $[0, 1/4]$. Second row: left - the windowed kernel $W_0(r)$; right - its Fourier transform. Third row: left - the difference kernel $D_0(r)$ that is numerically supported on $[0, 1]$; right - its Fourier transform. Fourth row: left - the difference kernel $D_1(r)$ that is numerically supported on $[0, 1/2]$; right - its Fourier transform. Note that the difference kernels D_1 is exactly a rescaled version of D_0 , with one half the support and twice the frequency content.

coarser levels, where B_0 is the unit box at level 0. Using (3.25) and (3.1), we have

$$(3.37) \quad \begin{aligned} u(\mathbf{x}_i) &= \underbrace{u^{\text{far}}(\mathbf{x}_i)} + \underbrace{\sum_{l=1}^{L-1} u_l^{\text{diff}}(\mathbf{x}_i)} + \underbrace{u_L^{\text{local}}(\mathbf{x}_i)} \\ &= \sum_{j=1}^N W_0(|\mathbf{x}_i - \mathbf{y}_j|) \rho_j + \sum_{l=0}^{L-1} \sum_{j=1}^N D_l(|\mathbf{x}_i - \mathbf{y}_j|) \rho_j + \sum_{j=1}^N R_L(|\mathbf{x}_i - \mathbf{y}_j|) \rho_j. \end{aligned}$$

Before describing a fast algorithm based on (3.37), we introduce some notation.

DEFINITION 3.5. Let $\mathbf{c}(B)$ denote the center of box B at level l . The outgoing expansion $\Phi_l(B)$ for box B has N_F elements, indexed by

$$(3.38) \quad [\Phi_l(B)]_{\mathbf{m}} = \sum_{\mathbf{y}_j \in B} e^{-i h_l \mathbf{k}_{\mathbf{m}} \cdot (\mathbf{y}_j - \mathbf{c}(B))} \rho_j, \quad \mathbf{m} \in [-n_f, \dots, n_f]^3.$$

LEMMA 3.6. Suppose that B is a box containing a target \mathbf{x}_i at level l . The incoming expansion $\Psi_l(B)$ has N_F elements, indexed by

$$(3.39) \quad [\Psi_l(B)]_{\mathbf{m}} = \sum_{S \in C(B)} w_{l, \mathbf{m}} e^{i h_l \mathbf{k}_{\mathbf{m}} \cdot (\mathbf{c}(B) - \mathbf{c}(S))} \Phi_l(S)[\mathbf{m}], \quad \mathbf{m} \in [-n_f, \dots, n_f]^3,$$

where $w_{l, \mathbf{m}}$ is given by (3.35). Then

$$(3.40) \quad u_l^{\text{diff}}(\mathbf{x}_i) = \sum_{\mathbf{m} \in [-n_f, \dots, n_f]^3} e^{i h_l \mathbf{k}_{\mathbf{m}} \cdot (\mathbf{x}_i - \mathbf{c}(B))} [\Psi_l(B)]_{\mathbf{m}}.$$

This result follows immediately from (3.34) and the fact that translation of an expansion in exponentials is in diagonal form.

DEFINITION 3.7. The colleagues of a box B at level l will be denote by $C(B)$ and the number of boxes in $C(B)$ will be denoted by $N_C(B)$. ($N_C(B)$ is clearly bounded by 3^d .)

Informal description of the $O(N \log N)$ algorithm

- (i). Sort sources and targets on an adaptive level-restricted tree. Let L_{\max} denote the finest level.
- (ii). Initialize the field $u(\mathbf{x}_i)$ by computing the first term u^{far} in (3.37) directly, as in (3.21), except that N_F is given by (3.36), and independent of N . [This requires $O(N N_F)$ work. Using the type-1 and type-2 NUFFTs, this can be reduced to $O(N_F \log N_F + N \log^d(1/\epsilon))$ work, as in the discussion of the classical Ewald method above.]
- (iii). For every level $l = 1, \dots, L_{\max}$, compute the outgoing expansions $\Phi_l(B)$ for each non-leaf box B containing sources at that level. [Using direct methods, this again requires $O(N N_F)$ work. With the type-1 NUFFT, the cost can be reduced to $O(N + N_F \log N_F)$ work with a precision-dependent constant.]
- (iv). For every level $l = 1, \dots, L_{\max}$, for each non-leaf box B at that level, convert the outgoing expansion to an incoming expansion in each of its colleagues C that contains targets and add to $\Psi_l(B)$. [This requires at most $O(3^d N_F)$ work per box.]

- (v). For every level $l = 1, \dots, L_{\max}$, evaluate the sum (3.40) for each target \mathbf{x}_i if it lies in a box with an incoming expansion and add to field $u(\mathbf{x}_i)$. [Using direct methods, this again requires $O(NN_F)$ work. With the type-2 NUFFT, the cost can be reduced to $O(N + N_F \log N_F)$ work with a precision-dependent constant.]
- (vi). For every level $l = 1, \dots, L_{\max}$, for every source \mathbf{y}_j , which is contained in a leaf box B at level l , for each target \mathbf{x}_i in a colleague $C(B)$ or coarse neighbor $\mathcal{N}(B)$, increment the potential with the local contribution:

$$(3.41) \quad u(\mathbf{x}_i) = u(\mathbf{x}_i) + R_l(|\mathbf{x}_i - \mathbf{y}_j|)\rho_j.$$

In the adaptive setting, counting direct interactions requires some care, but it can be shown that the total number of direct interactions is of the order $O(N)$ (see [15, 58] for more details). In fact, uniform distributions are typically the setting where the direct cost is the greatest. It is worth noting that additional savings can be had by observing that the residual kernel R_l is negligible beyond a ball of radius r_l . Thus, in the simplest case where there are approximately n_s targets in each of 3^d colleagues, the relevant targets for each source \mathbf{y}_j are only those contained in the sphere of radius r_l centered at \mathbf{y}_j . Thus, the average number of targets with a nonzero contribution from a given source is approximately $\frac{4\pi}{3}n_s$ rather than $27n_s$. Finally, we recall that if a target is coincident with one of the sources, it should be omitted in the direct calculation and the self-interaction correction $u_{\text{self}}(\mathbf{x}_i)$ should be added to the potential $u(\mathbf{x}_i)$.

Without carrying out a detailed operation count, assuming $L_{\max} = O(\log N)$, this adaptive, multilevel extension of Ewald summation requires $O(N)$ work at each of $O(\log N)$ levels.

REMARK 3.8. *Kernel-splitting by itself is not new. It is the basis for the multilevel summation methods in [12, 13, 44, 45, 50, 67]. However, those methods rely on the evaluation of the smooth, difference kernel interactions through low-rank approximations in physical space. (Of note is the recent paper [57] which uses a sum-of-Gaussian approximation of the difference kernel and direct convolution in physical space using separation of variables for each individual Gaussian.) DMK is a dual-space method, like Ewald summation, making use of the Fourier transform to diagonalize these interactions with a significant cost savings. Diagonal translation plays a role in some existing kernel-independent FMMs, such as [77] and [78], where Fourier-based convolution is used to account for well-separated interactions.*

3.3. The linear scaling full DMK algorithm. In the scheme just outlined, we were obliged to carry out $O(N)$ operations at each of $\log N$ levels. In order to obtain an $O(N)$ scheme, we will need to develop a two-pass version of the method (as in multilevel summation or the FMM). Instead of step (ii), we will begin at the level of leaf nodes and construct a set of *proxy* charges at all coarser levels that give rise to the same field as the original source distribution. This will constitute an “upward pass” (see Figure 3.5). In the subsequent downward pass, rather than steps (iii) and (iv) above, where the difference kernel contributions are evaluated at every level, we convert the incoming field expressed in terms of complex exponentials into an expansion in Chebyshev polynomials. We then interpolate the Chebyshev expansion obtained in each parent box to its 2^d children and continue that process recursively

until a leaf node is reached. Only then is the Chebyshev expansion evaluated at the target locations (as in step (v) above). In this manner, we access each source and target point only $O(1)$ times, independent of the depth of the tree.

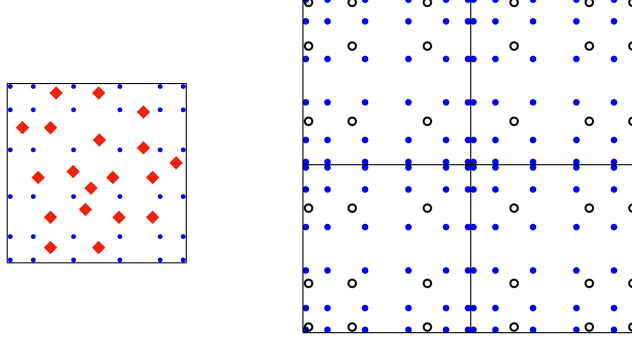


Fig. 3.5: In the $O(N)$ scheme, we construct a hierarchy of “proxy” charges to account for interactions at coarser and coarser scales. (Left) At the level of leaf nodes, we first build a tensor product Chebyshev grid of proxy charges (solid blue circles) with fields equivalent to those induced by the original sources themselves (red diamonds), illustrated in two dimensions. The cost of obtaining proxy charges from arbitrary charge locations requires $O(Np^d)$ work in d dimensions, where N is the number of sources. (Right) In the upward pass, we translate the tensor product of proxy charges on each child (solid blue circles) to a single tensor product of proxy charges at the level of the parent box (open black circles). The parent proxy grid is responsible for approximating smoother interactions at its own level.

Since the convolution kernels are smooth, we may use the antepolation approach described in subsection 2.2, illustrated in Figure 3.5. That is, in every leaf node, we replace the charges $\{\rho_j\}$ with a tensor product grid of equivalent sources (“proxy charges”) which give rise to the same smooth potential over the range of interest. At each coarser level, the 2^d tensor product grids of proxy charges are merged into a single tensor product grid, according to Lemma 2.2. This eliminates the $O(N \log N)$ cost incurred in the simpler scheme above, where some expansion is created from each source at each level.

DEFINITION 3.9. *The operator mapping the child proxy grid to the parent proxy grid will be denoted by T_{c2p} . T_{c2p} is simply the (multi-index) antepolation matrix U^T where U is defined in (2.1).*

Given the proxy charges on a tensor product grid, it is straightforward to compute outgoing expansion for a box B using a modified version of (3.38):

$$(3.42) \quad [\Phi_l(B)]_{\mathbf{m}} = \sum_{\mathbf{j} \in [1, \dots, p]^d} e^{-i h_l \mathbf{k}_{\mathbf{m}} \cdot (\mathbf{r}_{\mathbf{j}} - c(B))} \tilde{\rho}_{\mathbf{j}}, \quad \mathbf{m} \in [-n_f, \dots, n_f]^3,$$

where $\{\mathbf{r}_{\mathbf{j}}\}$ are the scaled tensor product Chebyshev nodes centered on B . Using separation of variables, the cost is of the order $O(pn_f^d)$.

We will also need to eliminate the $O(N \log N)$ cost incurred by evaluating the difference potential $u_{l,\text{diff}}$ at each target at each level. For this, once the incoming

expansion has been obtained for a box B , we compute the corresponding Chebyshev approximation $\Lambda_l(B)$:

$$(3.43) \quad u_l^{\text{diff}}(\mathbf{x}) = \sum_{\mathbf{m} \in [1, \dots, p]^d} \lambda_{l, \mathbf{m}} T_{\mathbf{m}-1}(\mathbf{x})$$

with expansion coefficients

$$(3.44) \quad \lambda_{l, \mathbf{m}} = \sum_{\mathbf{n} \in [1, \dots, p]^d} U(\mathbf{m}, \mathbf{n}) u_l(\tilde{\mathbf{r}}_{\mathbf{n}}).$$

Here, $\tilde{\mathbf{r}}_{\mathbf{n}}$ are the shifted and scaled Chebyshev grid on the target box. The values $u_l(\tilde{\mathbf{r}}_{\mathbf{n}})$ are themselves obtained using separation of variables by evaluating

$$(3.45) \quad u_l^{\text{diff}}(\mathbf{r}_{\mathbf{n}}) = \sum_{\mathbf{m} \in [-n_f, \dots, n_f]^3} e^{i h_l \mathbf{k}_{\mathbf{m}} \cdot (\mathbf{r}_{\mathbf{n}} - \mathbf{c}(B))} [\Psi_l(B)]_{\mathbf{m}}.$$

The cost involved is of the order $O(p n_f^d + p^2 n_f^{d-1} + \dots + p^d n_f)$. Since n_f is generally larger than p , we will refer to this cost as of the order $O(p n_f^d)$.

For non-leaf boxes, as in the FMM, we do not evaluate the local expansions $\Lambda_l(B)$ directly. Instead, we translate the local expansions from B to its children. The translation operator converting the local expansions from the parent box to the child box is given by the formula

$$(3.46) \quad T_{p2c} = V^{-1} E$$

from [Lemma 2.3](#) and [\(2.10\)](#). It is easy to see that both T_{c2p} and T_{p2c} are independent of the level in the tree hierarchy and that there are 2^d such operators in \mathbb{R}^d .

For a target \mathbf{x} in a leaf box B at level L , we define the *far-field potential* as the sum of the windowed kernel interactions and the difference kernel interactions up to that level:

$$(3.47) \quad u_L^{\text{far}}(\mathbf{x}) = u^{\text{smooth}}(\mathbf{x}) + \sum_{l=0}^{L-1} u_l^{\text{diff}}(\mathbf{x})$$

The far-field potential will be evaluated *once* for each target via standard (Chebyshev) interpolation. The near-field correction is

$$(3.48) \quad u_L^{\text{local}}(\mathbf{x}) = \sum_{\mathbf{y}_j \in C(B)} R_L(|\mathbf{x} - \mathbf{y}_j|) \rho_j + \sum_{\mathbf{y}_j \in \mathcal{N}(B)} R_{L-1}(|\mathbf{x} - \mathbf{y}_j|) \rho_j \\ + \sum_{\mathbf{y}_j \in \mathcal{F}(B)} R_{L+1}(|\mathbf{x} - \mathbf{y}_j|) \rho_j,$$

where $\mathcal{N}(B)$ and $\mathcal{F}(B)$ are the coarse and fine neighbors of B , respectively.

REMARK 3.10. *Note that the residual kernel index (in R_L , R_{L-1} or R_{L+1} above) is tied to the level of refinement of the source box since the far field contribution for that source may have terminated at a coarser level. The union of $C(B)$, $\mathcal{N}(B)$, and $\mathcal{F}(B)$ is exactly the so-called list 1 in the adaptive FMM (see, for example, [\[20\]](#)).*

3.4. Reducing the cost of direct interactions. In the DMK framework (as with FMMs and other linear scaling multilevel schemes), the optimal tree depth is achieved when the cost of direct interactions, here with the residual kernel, balances the cost of far field interactions. Thus, accelerating direct interactions has a significant effect on the overall performance. As noted in the paragraph before [Remark 3.8](#), we can reduce the number of targets that need to be considered by exploiting the fact that the residual kernel R_L is negligible beyond a ball of radius r_L about any source at level L . As illustrated in the right-hand diagram of [Figure 3.1](#), we can easily reduce the search for targets by refining every box *once*. Consider a source \mathbf{y}_j that lies in the box B in the left-hand diagram of [Figure 3.1](#). To see which targets are relevant, pairwise distances would have to be computed throughout B 's colleagues and coarse neighbors. With an additional level of refinement, however, suppose \mathbf{y}_j is determined to lie in the indicated child box B_a . We can then restrict the distance calculation to the colleagues and coarse neighbors of B_a and only the subset of boxes indicated in pale green. The remaining targets are all outside the relevant ball of radius r_L centered on \mathbf{y}_j .

For the case of a uniform distribution, note that the number of boxes within the interaction range is 5^d at level $L + 1$ rather than 3^d boxes at level l . This reduces the number of distance calculations per source from $3^d n_s$ to $5^d (n_s / 2^d) = 2.5^d n_s$. Furthermore, the pale green boxes are well separated from B_a and the residual kernel for targets in those boxes is smooth and easily approximated by a polynomial of one variable in r (or r^2). This avoids the need for evaluating special functions (such as $\text{erf}(r/\sigma)$) for these interactions.

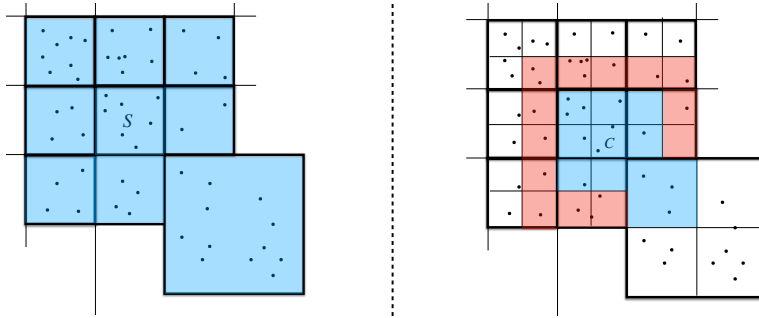


Fig. 3.6: Interaction lists due to the residual kernel. Left: the original list L_D as in [\[36\]](#). The list L_D of a leaf box S at level l contains all target boxes that are its neighbors at level l or leaf neighbors at level $l - 1$. Right: the target boxes that are in the interaction range of a child box C of S . Here, all leaf boxes are refined once more. Since the residual kernel R_l is zero outside a ball of radius $|B_l|$, only blue and red boxes have nonzero interactions with the source box C at level $l + 1$. Furthermore, red boxes are well separated from C . Thus, the residual kernel is smooth for the interaction between red target boxes and the source box C . The residual kernel in this range can be well approximated by a low degree polynomial of r^2 , avoiding the expensive calculation of special functions (including the square-root function). Finally, the self interaction is always carried out at level l (i.e., the parent box S) to reduce cache misses in SIMD vectorization.

3.5. The full DMK algorithm for discrete sources. We assume we are given a level-restricted adaptive tree on input, that has fewer than n_s sources and targets in

each leaf node. Constructing such a tree requires $O(N \log N)$ work (assuming there are $O(\log N)$ levels in the tree hierarchy). See [69] for further details. Each box B in the data structure is then assigned some logical flags.

1. If B is a leaf box, then $F_{\text{leaf}}(B) = 1$. Otherwise $F_{\text{leaf}}(B) = 0$.
2. If B contains more than n_s sources, $F_{\text{out}}(B) = 1$. Otherwise $F_{\text{out}}(B) = 0$.
3. If any of B 's colleagues contain more than n_s sources, $F_{\text{in}}(B) = 1$. Otherwise $F_{\text{in}}(B) = 0$.

As noted above, we carry out one additional refinement for all boxes to accelerate the direct interaction step. Thus, a box B which was a leaf node in the given data structure has $F_{\text{leaf}}(B) = 1$. The children under this additional refinement step are assigned $F_{\text{leaf}} = 0$.

The discrete (DMK) algorithm

Comment [On input, we are given a collection of N sources and targets \mathbf{x}_i , $i = 1, 2, \dots, N$ and \mathbf{y}_j , $i = 1, 2, \dots, N$, a prescribe precision ϵ , and a parameter n_s (the maximum number of points in a leaf box). On output, we return the potential at all target locations.]

Step 0: Initialization

- 1: Build a level-restricted adaptive tree using the algorithm (see, for example, [69]). The root box is denoted by B_0 , the maximum level is denoted L_{max} , and the total number of boxes is denoted N_{box} .
- 2: Initialize the potential $u(\mathbf{x}_i)$, $i = 1, \dots, N$ to zero.
- 3: Calculate δ_1 according to the prescribed precision ϵ .
- 4: Compute the Fourier expansion length $N_F^{(0)}$ for the windowed kernel W_0 , the Fourier expansion length $N_F = (2n_f + 1)^3$ for the difference kernels D_l , $l = 0, \dots, L_{\text{max}} - 1$, and the polynomial approximation order p in each dimension based on the prescribed precision ϵ .
- 5: Compute the flags $F_{\text{leaf}}(B)$, $F_{\text{out}}(B)$, $F_{\text{in}}(B)$, for each box B in the tree.
- 6: Carry out one additional refinement for each leaf node (assigning these additional boxes the flags $F_{\text{leaf}}(B) = F_{\text{out}}(B) = F_{\text{in}}(B) = 0$).

Step 1: Precomputation

Comment [Create transformation and translation matrices.]

- 1: Compute the 2^d translation matrices T_{c2p} and T_{p2c} according to Lemma 2.2 and Lemma 2.3.
- 2: Compute the transformation matrix T_{prox2pw} converting proxy charges into the outgoing plane wave expansions from (3.42) and the transformation matrix T_{pw2poly} converting incoming plane wave expansions into local expansions, from (3.45), (3.44). By translation invariance, only one matrix is needed for each level. Using separation of variables, it is easy to see that one only needs to store one-dimensional matrices of size $(2n_f + 1) \times p$.
- 3: Compute the translation matrices T_{pwshift} converting outgoing plane wave expansions of a source box into incoming plane wave expansions of its colleagues from (3.39). There are 3^d of them for each level.

Step 2: Upward pass

Comment [For each leaf box, form the proxy charges from the original sources.]

```

for each box  $B_i, i = 1, \dots, N_{\text{box}}$  do
  if  $F_{\text{leaf}}(B_i) = 1$  then
    Form proxy charges  $\tilde{\rho}_m(B)$  from sources via (2.8).
  end if
end for

for level  $l = L_{\text{max}-1}, \dots, 0$  do
  for each box  $B$  at level  $l$  do
    if  $B$  is a parent box then
      Form the proxy charges from proxy charges in children using  $T_{c2p}$ .
    end if
  end for
end for

```

Step 3: Downward pass

```

for level  $l = 0, \dots, L_{\text{max}-1}$  do
  for each box  $B$  at level  $l$  do                                      $\triangleright$  Form outgoing expansions
    if  $F_{\text{out}}(B) = 1$  then
      Form the outgoing expansion  $\Phi_l(B)$  for the difference kernel  $D_l$  from the
      proxy charge expansion coefficients using  $T_{\text{prox}2\text{pw}}$ .
    end if
  end for

  for each box  $B$  at level  $l$  do                                      $\triangleright$  Form incoming expansions
    if  $F_{\text{in}}(B) = 1$  then
      for each box  $B_n$  in  $C(B)$  do
        if  $F_{\text{out}}(B_n) = 1$  then
          Translate the outgoing expansion  $\Phi_l(B_n)$  to the center of  $B$  and
          add to the incoming plane wave expansion  $\Psi_l(B)$  using  $T_{\text{pwshift}}$ .
        end if
      end for
    end if
  end for

  for each box  $B$  at level  $l$  do                                      $\triangleright$  Form local expansions
    if  $F_{\text{in}}(B) = 1$  then
      Convert incoming plane wave expansion  $\Psi_l(B)$  to the local expansion
       $\Lambda_l(B)$  using  $T_{\text{pw}2\text{poly}}$ .
    end if
  end for

  for each box  $B$  at level  $l$  do                                      $\triangleright$  Split local expansions
    if  $F_{\text{in}}(B) = 1$  then
      for each child box  $C$  of  $B$  do
        Translate and add the local expansion of  $B$  to the local expansion of
         $C$ .
      end for
    end if
  end for

```

```

    end for
  end if
end for

for each box  $B$  at level  $l$  do
  if  $F_{\text{leaf}}(B) = 1$  then
    Evaluate the mollified potential  $u_L^{\text{far}}$  at each target  $\mathbf{x}$  in  $B$ .
  end if
end for
end for

```

Step 4: Compute direct interactions

```

for level  $l = 0, \dots, L_{\text{max}}$  do
  for each box  $B$  at level  $l$  do
    if  $B$  is a leaf box then
      Compute the local contribution to the potential  $u_i^{\text{local}}$  at all targets in
      the colleagues of  $B$  due to all sources in  $B$  directly and add to the potential. The
      search for targets in this step is accelerated by carrying out the processing using
      the refined leaf nodes (see subsection 3.4).
    end if
  end for
end for

```

Step 5: Self-interaction corrections

```

for  $l = 0, \dots, L_{\text{max}}$  do
  for each leaf box  $B$  at level  $l$  do
    for each target  $\mathbf{y}_j$  in  $B$  do
      If target  $\mathbf{x}_i$  is coincident with a source  $\mathbf{y}_j$ , compute the self-interaction
      term  $u^{\text{self}}(\mathbf{x}_i)$  in (3.5) and add to  $u(\mathbf{x}_i)$ .
    end for
  end for
end for

```

3.5.1. Complexity analysis. Let n_f be the Fourier expansion length of the difference and windowed kernels in each dimension, and let p be the polynomial approximation order for these kernels in each dimension. (In general, $n_f > p$, so that terms of the form $pn_f^d + p^2n_f^{d-1} + \dots + p^dn_f$ are dominated by pn_f^d .) It is straightforward to verify that

- The construction of the proxy charges on leaf boxes requires $O(p^d)$ work per source.
- The translation of proxy charges from child to parent requires $O(dp^{d+1})$ work per box.
- The evaluation of outgoing expansions from proxy charges requires $O(dpn_f^d)$ work per box.
- The translation from outgoing expansions to incoming expansions requires $O(3^dn_f^d)$ work per box.

- The computation of local expansions from incoming expansions requires $O(dpn_f^d)$ work per box.
- The translation of local expansions from parent to child requires $O(dp^{d+1})$ work per box.
- The evaluation of the mollified potential requires $O(p^d)$ work per target.
- The evaluation of the local potential requires $O(3^d n_s)$ work per target.

Thus, the total cost C is given by

$$(3.49) \quad C = O(3^d n_s N + 2p^d N + 2dp^{d+1} N_{\text{box}} + 2dpn_f^d N_{\text{box}} + 3^d n_s^d N_{\text{box}}).$$

In the case of uniform distributions, N_{box} is bounded by $2N/n_s$, leading to $O(N)$ complexity. For general distributions, the proof of linear complexity (after sorting) is similar to that in [58] for the FMM. BLAS level 3 subroutines such as DGEMM and ZGEMM.

REMARK 3.11. *The first term on the right hand side of (3.49) involves the evaluation of special functions and has a large prefactor implicit in the $O(N)$ notation. All of the other terms have very small associated constants and many of the steps are compatible with optimized linear algebra (BLAS) routines. As observed above, the prefactor 3^d in the direct evaluation step with residual kernels can be accelerated by looking only within a sphere of radius r_L centered on a source at level L . This reduces the volume to π instead of 9 in 2D and $4\pi/3$ instead of 27 in 3D. In practice, this makes it harder to use “SIMD” vectorization on modern architectures.*

REMARK 3.12. *The parameter n_s should be chosen so that the cost of local interactions and the cost of all other steps are roughly balanced. In our implementation, we optimize the selection of n_s by experimentation with sources distributed on a surface.*

3.6. Modification of DMK for continuous sources. We now consider the evaluation of the volume potential (1.2) for the specific case of the Laplace kernel:

$$(3.50) \quad u(\mathbf{x}) = \int_{B_0} \frac{1}{|\mathbf{x} - \mathbf{y}|} \rho(\mathbf{y}) d\mathbf{y},$$

where B_0 is the unit cube $[-1/2, 1/2]^3$, and the density ρ is assumed to be smooth on B_0 . The first task is to build a level-restricted adaptive tree that resolves the density ρ to precision ϵ . That is, we keep refining the tree until the density is approximated by a tensor product polynomial of degree $\leq q - 1$ on each leaf box B to the desired precision:

$$(3.51) \quad \rho(\mathbf{x}) \approx \sum_{j \in [1, \dots, q]^d} c_j P_{j-1}(\mathbf{x}), \quad \mathbf{x} \in B,$$

where we have switched from Chebyshev to Legendre polynomials for convenience when computing integrals (see subsection 2.1).

3.6.1. Creating proxy charges. The changes to the code in terms of the far-field interactions are very minor. We focus on the difference kernel D_l here. The windowed kernel at level 0 is treated in the same way. For a leaf box B , we need to evaluate integrals of the form

$$(3.52) \quad u_l^{\text{diff}}(\mathbf{x}) = \int_B D_l(|\mathbf{x} - \mathbf{y}|) \rho(\mathbf{y}) d\mathbf{y}.$$

We have seen above that D_l is well-approximated by a polynomial of order p . Assuming $q \leq p$, the integral in (3.52) can be computed accurately using tensor product Gauss-Legendre quadrature of order p since it is exact for polynomials of degree up to $2p$. That is,

$$(3.53) \quad u_l^{\text{diff}}(\mathbf{x}) \approx \sum_{\mathbf{n} \in [1, \dots, p]^d} \left(\frac{r_l}{2}\right)^d w_{\mathbf{n}} D_l(\mathbf{x}, \mathbf{q}_{\mathbf{n}}) \rho(\mathbf{q}_{\mathbf{n}}),$$

where r_l is the linear dimension of B , the points $\{\mathbf{q}_{\mathbf{n}}\}$ are the tensor product Legendre nodes (see subsection 2.1), and $w_{\mathbf{n}}$ are the weights of the standard tensor-product Gauss-Legendre quadrature rule scaled to B . Thus, the proxy charges for a leaf node are

$$\tilde{\rho}_{\mathbf{n}} = \left(\frac{r_l}{2}\right)^d w_{\mathbf{n}} \rho(\mathbf{q}_{\mathbf{n}}).$$

This requires evaluation of the Legendre expansion (3.51) at the p^d tensor-product Legendre nodes at a cost of $O(qp^d)$ work using separation of variables - much less work than in the discrete case.

Likewise, when evaluating the local expansions in Step 3 of the algorithm, the targets lie on a tensor-product grid, so that the cost is of the order $O(qp^d)$ work rather than $O(q^d p^d)$. Amortized over the q^d discretization points needed to represent $\rho(\mathbf{x})$, this amounts to a cost of the order $O(Nq(p/q)^d)$ work instead of $O(Np^d)$ - a significant reduction.

3.6.2. Approximation of the local interactions. Recall that, in the discrete setting, the direct calculations involve sums of residual kernel interactions R (3.26). In the continuous setting, these interactions involve integrals of singular functions and require some care. We will make use of the integral representation

$$(3.54) \quad R(r) = \frac{\text{erfc}(r/\sigma)}{r} = \frac{2}{\sqrt{\pi}} \int_{1/\sigma}^{\infty} e^{-r^2 t^2} dt = \frac{1}{\sqrt{\pi}} \int_0^{\sigma^2} \frac{e^{-r^2/s}}{s^{3/2}} ds,$$

which can be derived from (A.16) and the definition of erfc . We have dropped the level index L in the residual kernel here, since it is simply determined by the choice $\sigma = \sigma_L$. The formulas in (3.54) must be understood in a distributional sense, which is justified here since what we actually need to compute is integrals of the following form:

$$(3.55) \quad u^{\text{local}}(\mathbf{x}) = \int_B R(|\mathbf{x} - \mathbf{y}|) \rho(\mathbf{y}) d\mathbf{y}.$$

Without loss of generality, let B be the unit cube centered at the origin with σ chosen according to (3.28) as

$$(3.56) \quad \sigma \approx \frac{1}{\sqrt{\log(1/\epsilon)}}.$$

For readers familiar with FMM-based volume integral codes, recall that the local interactions are computed by tabulating integrals of the Green's function $1/r$ with each of q^d polynomial basis functions at each of q^d points within the box or its neighbors. Thus, the work required is of the order $O(q^{2d})$. In the DMK framework, we seek to exploit the compact support of the residual kernel and the formulas in (3.54), which we can interpret as a continuous sum-of-Gaussians (SOG) representation for

$R(r)$ involving more and more sharply peaked Gaussians as $\sigma \rightarrow 0$. We will actually truncate the integrals in (3.54), and write

$$(3.57) \quad R(r) = \frac{2}{\sqrt{\pi}} \int_{1/\sigma}^{1/\sigma_{\min}} e^{-r^2 t^2} dt = \frac{1}{\sqrt{\pi}} \int_{\sigma_{\min}^2}^{\sigma^2} \frac{e^{-r/s}}{s^{3/2}} ds, \quad r \in [\epsilon_0, 1],$$

where ϵ_0 is a free parameter and

$$(3.58) \quad \sigma_{\min} = \sigma \epsilon_0 \approx \frac{\epsilon_0}{\sqrt{\log(1/\epsilon)}}.$$

It is easy to check that for $r \in [\epsilon_0, 1]$ the resulting error in (3.57) is of the order $O(\epsilon)$. We then seek a discrete SOG approximation of $R(r)$ of the form

$$(3.59) \quad R(r) \approx \sum_{i=1}^{n_g} w_i e^{-r^2 t_i^2}, \quad r \in [\epsilon_0, 1],$$

The choice of ϵ_0 is somewhat involved and discussed below. Given ϵ_0 , however, there are many ways of constructing the SOG approximation in (3.59). See, for example, [10] or the black-box algorithm in [37]. Combined with the application of generalized Gaussian quadrature [52, 76, 14], one obtains an SOG approximation with a number of terms of the order

$$(3.60) \quad n_g = O(\log(1/\epsilon)).$$

Combining (3.59) and (3.55), we obtain

$$(3.61) \quad u^{\text{local}}(\mathbf{x}) = u_1^{\text{local}}(\mathbf{x}) + u^{\text{asympt}}(\mathbf{x}),$$

where

$$(3.62) \quad u_1^{\text{local}}(\mathbf{x}) = \sum_{i=1}^{n_g} w_i \int_B e^{-|\mathbf{x}-\mathbf{y}|^2 t_i^2} \rho(\mathbf{y}) d\mathbf{y}$$

and

$$(3.63) \quad u^{\text{asympt}} \approx \int_{|\mathbf{x}-\mathbf{y}| \leq \epsilon_0} \left(\frac{\text{erfc}(|\mathbf{x}-\mathbf{y}|/\sigma)}{|\mathbf{x}-\mathbf{y}|} - \sum_{i=1}^{n_g} w_i e^{-|\mathbf{x}-\mathbf{y}|^2 t_i^2} \right) \rho(\mathbf{y}) d\mathbf{y}.$$

For $u_1^{\text{local}}(\mathbf{x})$, each term in (3.62) can be computed using separation of variables in $O(dq^{d+1})$ operations. For the contribution $u^{\text{asympt}}(\mathbf{x})$, one can carry out the calculation explicitly using a Taylor expansion of the density $\rho(\mathbf{y})$. For illustration, using a fourth order Taylor series and integrating term by term, we obtain

$$(3.64) \quad \begin{aligned} u^{\text{asympt}}(\mathbf{x}) &= 4\pi\rho(\mathbf{x}) \left(I_0 - \sum w_i \int_0^{\epsilon_0} e^{-r^2 \delta_i} r^2 dr \right) \\ &+ \frac{2\pi}{3} \Delta\rho(\mathbf{x}) \left(I_2 - \sum w_i \int_0^{\epsilon_0} e^{-r^2/\delta_i} r^4 dr \right) \\ &+ \frac{\pi}{6} \Delta^2\rho(\mathbf{x}) \left(I_4 - \sum w_i \int_0^{\epsilon_0} e^{-r^2/\delta_i} r^6 dr \right) + O(\epsilon_0^8), \end{aligned}$$

where $I_n, n = 0, 2, 4$ are given by the formula

$$(3.65) \quad I_n = \int_0^{\epsilon_0} \operatorname{erfc}(x/\sigma) x^{n+1} dx,$$

and the error estimate $O(\epsilon_0^8)$ comes from the integration over the ball of radius ϵ_0 of the error term in the Taylor series approximation (of order $O(\epsilon_0^6)$) multiplied by $1/r$. The integrals in (3.64) are easily computed in terms of the error function. We are now able to choose ϵ_0 . We simply require (assuming the fourth order approximation for ρ) that $\epsilon_0^8 = O(\epsilon)$ for precision ϵ .

To summarize, the cost of local interactions is of the order $O(\log(1/\epsilon)dq^{d+1})$ for each pair of boxes, leading to a cost of approximately $O(3^d dq \log(1/\epsilon))$ per grid point. In place of (3.49), the total cost of the DMK algorithm for continuous sources is

$$(3.66) \quad C = O(3^d dq N + 2(p/q)^{d-1} N + 2dp^{d+1} N_{\text{box}} + 2dpn_f^d N_{\text{box}} + 3^d n_f^d N_{\text{box}}),$$

Here, N is the total number of grid points:

$$(3.67) \quad N = N_{\text{leaf}} q^d,$$

where N_{leaf} is the number of leaf boxes in the tree. In the tree construction for a continuous density, it is easy to check that the total number of boxes in the tree satisfies the bound

$$(3.68) \quad N_{\text{box}} \leq \frac{1}{1 - 2^{-d}} N_{\text{leaf}}.$$

Combining (3.66), (3.67), and (3.68), we obtain

$$(3.69) \quad C = O([3^d dq + 2(p/q)^{d-1} + 2dp(p/q)^d + 2dp(n_f/q)^d + 3^d(n_f/q)^d] N).$$

As noted above, when compared with FMM-based volume integral approaches, the advantage of the present method is the expression of the residual kernel in terms of a modest number of Gaussians, permitting separation of variables acceleration in the local interactions and a dramatic reduction in the storage of local tables (since all of the needed matrices are one-dimensional).

3.7. Optimization of kernel splitting using prolate spheroidal wave functions. The last general improvement we introduce in the DMK framework is a reduction in the number of quadrature nodes needed in (3.34). For this, we will abandon the kernel splitting in (3.26), which is closely related to the integral representation (A.16) which makes essential use of the fact that a Gaussian is rapidly decaying in both physical and Fourier space.

From the discussion thus far, the reader will note that the essential features of kernel splitting aren't specific to the Gaussian, but assume that

- (a) the windowed kernel is smooth and admits an efficient Fourier transform,
- (b) the difference kernels $D_l(r)$ are smooth, admit efficient Fourier transforms, and are compactly supported (to precision ϵ) in the ball of radius r_l , where r_l is the side length of the boxes at level l , and
- (c) the residual kernels are compactly supported (to precision ϵ) in the ball of radius r_l .

Fixing our domain to be the interval $[-1, 1]$, note that in order for a Gaussian of the form $e^{-\delta^2 r^2}$ to decay to ϵ outside the interval $[-1, 1]$, we need to choose

$$(3.70) \quad \delta = \sqrt{\log(1/\epsilon)}.$$

By (A.7), the corresponding Fourier transform can be windowed at

$$(3.71) \quad K_{\max} = 2 \log(1/\epsilon).$$

Thus, it is worth considering other options, such as ψ_0^c , the first prolate spheroidal wave function (PSWF) of order zero, discussed in Appendix A.6. For ψ_0^c to decay to ϵ outside $[-1, 1]$, we have that

$$(3.72) \quad c \approx \log(1/\epsilon).$$

By (A.25), the Fourier transform of ψ_0^c is $\lambda_0 \psi_0^c(k/c)$, i.e., its Fourier transform can be windowed at

$$(3.73) \quad K_{\max} = c \approx \log(1/\epsilon).$$

Comparing (3.71) with (3.73), we find that the number of Fourier modes needed to approximate ψ_0^c is roughly half that needed for the corresponding Gaussian. In d dimensions, this results in a reduction of the total number of Fourier modes by a factor of 2^d , all else being equal. In Figure 3.7, we plot the PSWF of order zero ψ_0^c and the corresponding Gaussian at six digits of accuracy on the interval $[-1, 1]$, as well as their Fourier transforms.

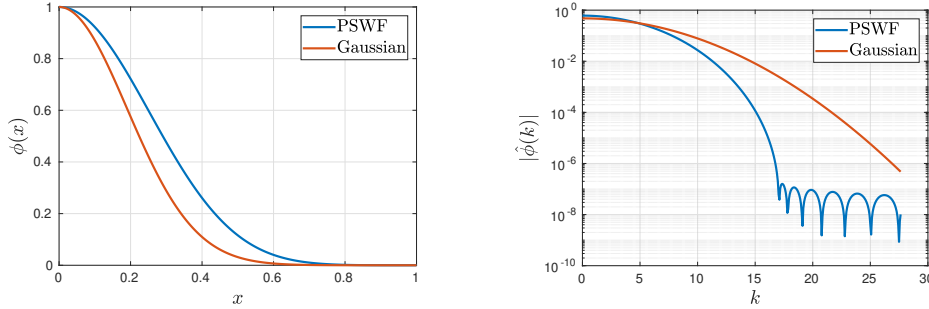


Fig. 3.7: Comparison of the Gaussian with the PSWF of order zero. Left: the scaled PSWF of order zero $\psi_0^c(x)/\psi_0^c(0)$ with $c = 16.893999099731445$ and the Gaussian $g(x) = e^{-\delta^2 x^2}$ with $\delta = \sqrt{\log(10^6)}$. The parameters c and δ are chosen such that $\psi_0^c(1) = g(1) = 10^{-6}$. Right: the Fourier transforms of the Gaussian and ψ_0^c . The Fourier transform of the latter decays much more rapidly than that of the former, requiring many fewer terms in the spectral approximation.

Using the function ψ_0^c , we propose an alternative kernel splitting. Letting

$$(3.74) \quad c_0 = \int_0^1 \psi_0^c(x) dx = \frac{1}{2} \hat{\psi}_0^c(0),$$

and

$$(3.75) \quad \Phi_l^c(r) = \frac{1}{c_0} \int_0^{r/r_l} \psi_0^c(x) dx,$$

the new windowed, difference, and residual kernels are defined by the formulas

$$(3.76) \quad \begin{aligned} W_0(r) &= \frac{\Phi_0^c(r)}{r}, \\ D_l(r) &= \frac{\Phi_{l+1}^c(r) - \Phi_l^c(r)}{r}, \\ R_L(r) &= \frac{1 - \Phi_L^c(r)}{r}. \end{aligned}$$

The corresponding splitting of the $1/r$ kernel is (repeating (3.25) here for convenience):

$$\frac{1}{r} = W_0(r) + \sum_{l=0}^{L-1} D_l(r) + R_L(r), \quad L = 0, 1, \dots, L_{\max},$$

which holds for any level L and any target in the unit box.

Since $\Phi_l^c(x) = 1$ for any $x \geq r_l$ by construction (to the desired precision), the difference and residual kernels in (3.76) are compactly supported on balls centered at the origin of radius r_l and r_L , respectively. Since ψ_0^c is an even function, both the windowed and difference kernels are smooth at the origin. Admittedly, the difference kernel $D_l(r)$ is not smooth at $r = r_{l+1}$ since $\psi_0^c(r/r_{l+1})$ has decayed only to ϵ and is extended beyond that range to zero. For the purpose of computation, however, this introduces an error of the order $O(\epsilon)$ in both physical and Fourier space and can be safely ignored. In short, the difference kernel admits an efficient Fourier transform and the new kernel splitting satisfies the three properties in subsection 3.7.

From the formulas in Appendix A.6, it is straightforward to show that the Fourier transform of the difference kernel is

$$(3.77) \quad \begin{aligned} \hat{D}_l(k) &= \frac{4\pi}{\psi_0^c(0)} \frac{\psi_0^c(|k|r_{l+1}/c) - \psi_0^c(|k|r_l/c)}{|k|^2}, \quad |k| \neq 0, \\ \hat{D}_l(0) &= \frac{2\pi c_2}{c_0} (r_l^2 - r_{l+1}^2), \quad c_2 = \int_0^1 x^2 \psi_0^c(x) dx. \end{aligned}$$

and that the Fourier transform of the windowed kernel is

$$(3.78) \quad \widehat{W}_0(k) = 4\pi \left(\frac{\sin((1+C)r_0 k/2)}{k} \right)^2 \hat{\phi}_0^c(|k|).$$

Table 3.1 lists the actual values of c in ψ_0^c , the number of quadrature nodes $N_1 = (2n_f + 1)$ needed to discretize the Fourier transform for the difference kernels, and the value p used to define the order of the polynomial representing the far field potential as well as the number of proxy charges in each linear dimension. We also show the grid spacing needed for the trapezoidal rule discretization of the difference kernels in the Fourier domain.

The cost of computing the residual kernels is more or less identical, since the evaluation of either Φ_l^c or erfc is most efficiently done by polynomial (or piecewise polynomial) approximation of the kernel from a pre-computed, one-dimensional table of values using Estrin's method [26]. The number of terms required in the polynomial approximation of Φ_l and erfc are more or less identical.

4. The DMK framework for general kernels. Most of the steps in the DMK algorithm are both dimension-independent and kernel-independent, since the

Table 3.1: Parameters used in the PSWF kernel splitting for the 3D Laplace kernel. ϵ is the desired precision, c is the computed PSWF parameter for the indicated value of ϵ , N_1 is the total number of Fourier modes in each dimension for ψ_0^c , p is the polynomial approximation order needed, and h_0 is the grid spacing in Fourier space for the difference kernel D_0 , respectively. At level l , $h_l = 2^l h_0$ and $K_{max} = 2^l c$. Note that h_0 is very close to the analytic formula (3.31), namely $4\pi/3$. For comparison, we also list N_1^G (the total number of Fourier modes in each dimension for the original splitting using Gaussians) and p^G (the associated polynomial approximation order for the difference kernels) in the last two columns.

ϵ	$ \log(1/\epsilon) $	c	$ N_1 $	p	h_0	$ N_1^G $	p^G
10^{-3}	6.9	7.2462000846862793	13	9	1.3240π	22	16
10^{-6}	13.8	13.739999771118164	25	18	1.3372π	44	30
10^{-9}	20.7	20.736000061035156	39	28	1.3250π	66	46
10^{-12}	27.6	27.870000839233398	53	38	1.3354π	88	62

mollified interactions are dealt with using the Fourier transform and polynomial approximation. For each kernel, however, the user must develop a telescoping series the requisite properties in subsection 3.7. For each such kernel-splitting formalism, its Fourier transform must be obtained and an accurate estimate of the quadrature for the spectral representation. While we do not attempt to provide a complete theory here, we show by example that the DMK framework is applicable and effective for a broad class of kernels. Note that, once the kernel is expressed as the sum of a windowed kernel and a residual kernel based on a parameter σ , the difference kernels can simply be define as the difference of windowed kernels at two successive scales (as in (3.27)).

4.1. Smooth kernels. If the kernel function $K(r)$ is smooth, then kernel splitting is particularly simple. Letting $w(x)$ be a smooth bump function supported on $[-1, 1]$ to the desired precision (such as a suitably scaled Gaussian or PSWF), we can simply write

$$(4.1) \quad K(r) = M_l(r) + R_l(r) := K(r)(1 - w(r/\sigma_l)) + K(r)w(r/\sigma_l).$$

Here, M_l is the mollified kernel and R_l is the residual kernel, which is compactly supported in the ball of radius σ_l . σ_l , as in the DMK method described in detail above, is a parameter that depends on the precision ϵ and level l . The efficiency of the splitting depends largely on two factors: how efficiently can we compute the residual kernel R_l and how many points are needed in the spectral representation of the difference kernel $D_l = M_{l+1} - M_l$. These are kernel-specific issues for which it is difficult to develop a general theory, although both theory and numerical experiments suggest that the PSWF ψ_0^c is a better choice of a window function than a Gaussian (see the discussion in subsection 3.7).

4.2. Singular, slowly decaying kernels. Let us now consider long range, translation invariant kernels $K(r)$ which have a singularity at the origin. By duality, their Fourier transforms are also singular at or near the origin and slowly decaying. The essential requirement in constructing a hierarchical splitting scheme with the properties enumerated in subsection 3.7 is to find a sequence of mollified kernels $S_l(r)$ with two properties:

1. $S_l(r)$ is smooth
2. $S_l(r) = K(r)$ for $r \geq r_l$ to the requested precision ϵ .

There are a number of methods one can use for this purpose, illustrated with specific examples in the following sections, where we exploit known integral representations, sum-of-Gaussian approximations, etc. If the Fourier transform $\widehat{K}(k)$ is known, one can also multiply by a suitable sequence of “filters” in the Fourier domain, yielding a fairly general approach. We present an example in [subsection 4.6](#).

In this section, we point out that there are purely numerical methods which can be used for this construction as well, without knowledge of the Fourier transform. One of these is to define $S_l = K(r)$ for $r \geq r_l$, and to use a smooth extension algorithm to fill in function values on $[0, r_l]$ to enforce some degree of smoothness, such as with the function extension method in [\[25\]](#) which can enforce C^n smoothness. For n sufficiently large, the Fourier transform can be computed numerically and decays rapidly enough that the trapezoidal rule is highly accurate.

One could also construct a sequence of smooth kernels $S_l(r)$ by convolution in physical space with a hierarchy of carefully chosen Gaussians or other *approximations to the identity* [\[68\]](#). We do not investigate these options in the present paper, focusing on the kernels for which other approaches are easily available.

Once we have constructed S_l , the kernel splitting takes the standard form

$$(4.2) \quad K(r) = W_0(r) + \sum_{l=0}^{L-1} D_l(r) + R_L(r), \quad L = 0, 1, \dots, L_{\max},$$

where

$$(4.3) \quad \begin{aligned} W_0(r) &= S_0(r)w(r), \\ D_l(r) &= S_{l+1}(r) - S_l(r), \\ R_L(r) &= K(r) - S_L(r). \end{aligned}$$

Since the difference kernels D_l are compactly supported in physical space, they are smooth in Fourier space (by the Paley-Wiener theorem) and the trapezoidal rule is spectrally accurate. For $W_0(r)$, we also need a smooth window function $w(r)$ such that $w(r) = 1$ for $|r| \leq \sqrt{d}r_0$ and $w(r) = 0$ for, say, $r > 2r_0$. Such a window function enforces rapid decay of the Fourier transform of W_0 . In short, kernel splitting in the general case involves hierarchical smoothing coupled with windowing at the coarsest level.

4.3. Kernels with known integral representations. In [Appendix A.4](#), we have listed a collection of kernels for which there are known integral representations involving Gaussians. Each of these integral representations provides a natural formalism for kernel-splitting. In general, suppose that the kernel $K(r)$ admits the following integral representation:

$$(4.4) \quad K(r) = \int_0^\infty s(t)e^{-r^2t^2} dt$$

for some weight function $s(t)$. (The integral representations listed in [Appendix A.4](#) are all of this form.) Then the multilevel kernel splitting of $K(r)$ can be accomplished using Gaussians:

$$(4.5) \quad K(r) = M_0(r) + \sum_{l=0}^{L-1} D_l(r) + R_L(r), \quad L = 0, 1, \dots, L_{\max},$$

where

$$(4.6) \quad \begin{aligned} M_0(r) &= \int_0^{\delta_0} w(t)e^{-r^2 t^2} dt, \\ D_l(r) &= \int_{\delta_l}^{\delta_{l+1}} w(t)e^{-r^2 t^2} dt, \\ R_L(r) &= \int_{\delta_L}^{\infty} w(t)e^{-r^2 t^2} dt, \end{aligned}$$

with $\delta_l = 1/\sigma_l$ and σ_l is given by (3.28).

REMARK 4.1. *The parameters δ_l get larger as one moves to finer levels, whereas the parameters σ_l get smaller. More precisely, σ_l is the length scale of a box and, in some respects, more natural. Many integral representations, however, are more easily written in the form (4.4), and we will use the inverse length scale δ_j for many kernels below.*

Care must be taken when constructing an efficient discrete Fourier approximation of M_0 . While M_0 is smooth in physical space, it may still have a far field which is not rapidly decaying, so that its Fourier transform could have some singular structure (typically at the origin for non-oscillatory kernels). One approach to finding a windowed function with the same value in the computational domain (say the unit box) is to calculate the Fourier representation of a truncated version of M_0 , with the truncation beyond the domain of interest. This is a topic discussed extensively in [74] and used above for the $1/r$ kernel (see Remark 3.3). Other specific examples will be discussed shortly.

4.4. Sum-of-Gaussians approximation. When an integral representation for a kernel is available in terms of Gaussians, as in the preceding section, finding a telescoping approximation is simply a matter of quadrature. When no such representation is available, however, one can begin by constructing an approximation of the form

$$(4.7) \quad K(r) = \begin{cases} \sum_{i=1}^{n_g} w_i e^{-r^2 t_i^2}, & r \in [\epsilon_0, \sqrt{d}r_0], \\ \sum_{i=1}^{n_g} w_i e^{-r^2 t_i^2} + K_{loc}(r) & 0 < r < \epsilon_0. \end{cases}$$

where r_0 is the side length of the box B_0 . The cut-off ϵ_0 is generally needed since many kernels of interest are singular at the origin.

Constructing such a sum of Gaussians (SOG) approximation on an interval bounded away from the origin is a well-studied (but nonlinear) task and closely related to approximation by sums of exponentials (SOE) and rational approximation and we refer the reader to the literature for further details (see, for example, [10, 35, 75]). Recently, attempts have been made to permit the ‘‘black-box’’ construction of SOG approximations (see, for example, [33, 37]).

Given the SOG approximation valid on $[\epsilon_0, \sqrt{d}r_0]$, kernel splitting can be achieved by defining the windowed, difference, and residual kernels as follows:

$$(4.8) \quad \begin{aligned} W_0(r) &= \sum_{t_i \leq \delta_0} w_i e^{-r^2 t_i^2}, \\ D_l(r) &= \sum_{\delta_l \leq t_i \leq \delta_{l+1}} w_i e^{-r^2 t_i^2}, \\ R_L(r) &= \sum_{t_i \geq \delta_L} w_i e^{-r^2 t_i^2}. \end{aligned}$$

Clearly, the difference and residual kernels are compactly supported with the correct support size (since $\delta_l = 1/\sigma_l$). Moreover, the windowed and difference kernels are smooth and admit efficient Fourier approximations.

More importantly, for continuous sources, we can exploit the representation of the residual kernel as a sum of Gaussians, as we did in [subsection 3.6](#), and accelerate the computation of local interactions using separation of variables. When t_i is very large, however, we can do even better. and compute the local interactions asymptotically but with controlled precision. For this, suppose we have expanded the density ρ as a Taylor series. We may then replace the finite domain of integration (over a leaf node and its colleagues) by integration over \mathbb{R}^d for any individual Gaussian $e^{-r^2 t_i^2}$ since the Gaussian has decayed to ϵ outside the colleagues at level L by construction (that is, $t_i \geq \delta_L$). To sixth order in σ , it is easy to check that

$$(4.9) \quad \int_{\mathbb{R}^d} e^{-|\mathbf{x}-\mathbf{y}|^2/\sigma} \rho(\mathbf{y}) d\mathbf{y} = (\pi\sigma)^d \left(\rho(\mathbf{x}) + \frac{\sigma^2}{4} \Delta \rho(\mathbf{x}) + \frac{\sigma^4}{32} \Delta^2 \rho(\mathbf{x}) + O(\sigma^6) \right).$$

Estimating the error term, the asymptotic expansion is accurate to the desired precision as soon as $(4\sigma^2/r_l^2)^3 < \epsilon$, where $\sigma = 1/t_i$. Thus, for values t_i in [\(4.8\)](#) that satisfy this criterion, we can bypass the table-based, separation of variables method to convolve with the Gaussian kernel and replace it with a calculation involving only a few floating point operations per target (once the Laplacian and bi-Laplacian have been applied to ρ).

We also need to account for the contribution of the local correction kernel K_{loc} in [\(4.7\)](#), which is supported on $[0, \epsilon_0]$:

$$(4.10) \quad \begin{aligned} & \int_{B_0} K_{loc}(\mathbf{x} - \mathbf{y}) \sigma(\mathbf{y}) d\mathbf{y} \\ &= \int_{\mathbf{x}+B_{\epsilon_0}} K_{loc}(r) \sigma(\mathbf{x} + \mathbf{y}) d\mathbf{y}. \end{aligned}$$

It is easy to see that the above integral can be reduced to a set of one-dimensional integrals on $[0, \epsilon_0]$ by expanding the density as a Taylor series in spherical coordinates and having access to integrals of the form

$$(4.11) \quad \int_0^{\epsilon_0} K_{loc}(r) r^k dr$$

These integrals are easily computed on the fly at negligible cost.

For discrete sources, [\(4.7\)](#) can still be used for kernel splitting, but the local interactions become expensive (without significant precomputation work) because of the large number of terms needed to evaluate the residual kernel.

4.4.1. Sum-of-Gaussians approximation for the Yukawa kernel. In general, one may obtain nearly optimal SOG approximation for a given kernel whose range is restricted to the computational domain by using generalized Gaussian quadrature [[14](#), [52](#), [76](#)]. This is particularly effective if this can be done in a precomputation step so that it does not dominate the total computational cost. For any given power function, this is easy to do (storing only the values $\{w_i, t_i\}$ in [\(4.7\)](#)). For the Yukawa kernel, this is not so straightforward because the tables are distinct for each value of the parameter λ in the kernel. Thus, we seek an SOG approximation that can be computed on the fly at negligible cost. For this, we use the change of variable $u = e^t$

in (A.17), which leads to

$$(4.12) \quad \begin{aligned} \frac{1}{2\pi} K_0(\lambda r) &= \frac{1}{2\pi} \int_{-\infty}^{\infty} e^{-r^2 e^{2u} - \frac{\lambda^2 e^{-2u}}{4}} du, \quad \mathbf{x} \in \mathbb{R}^2, \\ \frac{1}{4\pi} \frac{e^{-\lambda r}}{r} &= \frac{1}{2\pi^{3/2}} \int_{-\infty}^{\infty} e^{-r^2 e^{2u} - \frac{\lambda^2 e^{-2u}}{4} + u} du, \quad \mathbf{x} \in \mathbb{R}^3. \end{aligned}$$

Note that the integrands in (4.12) are exponentially decaying at $\pm\infty$ so that the windowed trapezoidal rule converges with spectral accuracy. When the parameter λ is very small, a more efficient optimization procedure related to the modified Prony method in [10] can be used to reduced the number of Gaussians for $u \in (-\infty, 0]$.

4.5. Kernel splitting of the general power function using PSWFs. Since, as we saw for the case $1/r$, it is generally more efficient to carry out kernel splitting with prolate spheroidal wave functions rather than Gaussians, we consider how to do so for the general power function. Other kernels can be treated in a similar fashion. For the general power function, its kernel splitting using ψ_0^c can be constructed as follows:

$$(4.13) \quad \frac{1}{r^\alpha} = M_0(r) + \sum_{l=0}^{L-1} D_l(r) + R_L(r), \quad L = 0, 1, \dots, L_{\max},$$

where

$$(4.14) \quad \begin{aligned} M_0(r) &= \frac{\Phi_0(r)}{r^\alpha}, \\ D_l(r) &= \frac{\Phi_{l+1}(r) - \Phi_l(r)}{r^\alpha}, \\ R_L(r) &= \frac{1 - \Phi_L(r)}{r^\alpha}, \end{aligned}$$

$$(4.15) \quad \Phi_l(r) = \int_0^r x^{\alpha-1} \phi_l(x) dx = \frac{1}{c_0} \int_0^{r/r_l} x^{\alpha-1} \psi_0^c(x) dx,$$

$$(4.16) \quad \phi_l(x) = \frac{1}{r_l^\alpha c_0} \psi_0^c\left(\frac{x}{r_l}\right), \quad c_0 = \int_0^1 x^{\alpha-1} \psi_0^c(x) dx.$$

In order to verify that the above construction satisfies the properties (a)-(c) in [subsection 3.7](#), we note that ψ_0^c is a smooth, even function. Substituting the Taylor expansion of ψ_0^c into (4.15), we obtain

$$(4.17) \quad \Phi_l(r) = \int_0^{r/r_l} x^{\alpha-1} \sum_{i=0}^{\infty} C_i x^i dx = \sum_{i=0}^{\infty} \frac{C_i}{i + \alpha} \left(\frac{r}{r_l}\right)^{\alpha+i}.$$

Thus, the windowed and difference kernels in (4.14) are smooth at the origin. The compactness of the residual kernel follows from the fact that $\Phi_L(r) = 1$ for $r \geq r_L$.

REMARK 4.2. *The above construction works well for $\alpha \in (0, 2]$ in the sense that the Fourier expansion length of the windowed and difference kernels defined in (4.14) does not differ much from that for the $1/r$ kernel. When α increases, it is better to use PSWFs with values of the parameter c different from those listed in [Table 3.1](#). This is because the parameter values there are chosen specifically for the $1/k^2$ kernel in Fourier space. As α increases, the Fourier transform of $1/r^\alpha$ decreases more slowly. We have not carried out any detailed analysis on this.*

4.5.1. An alternative kernel splitting for the $1/r^2$ kernel in three dimensions. The kernel $K(r) = \frac{1}{r^2}$ is the Green's function for the square root of the Laplacian in three dimensions, with Fourier transform $\widehat{K}(\mathbf{k}) = 2\pi^2/k$ (see (A.8) with $\alpha = 2$ and $d = 3$). In this section, we provide an alternative route to kernel splitting that relies on knowing \widehat{K} rather than using (4.13) with $\alpha = 2$. The resulting scheme has more or less the same performance - we introduce it here to show that there are many effective routes compatible with the DMK framework. The only subtle issue when manipulating the kernel in the Fourier domain is to ensure that the difference and residual kernels have the appropriate compact support in physical space. To be more precise, we write

$$(4.18) \quad \frac{1}{r^2} = M_0(r) + \sum_{l=0}^{L-1} D_l(r) + R_L(r), \quad L = 0, 1, \dots, L_{\max},$$

where

$$(4.19) \quad \begin{aligned} M_0(r) &= \frac{1 - \psi_0^c(r/r_0)/\psi_0^c(c)}{r^2}, \\ D_l(r) &= \frac{\psi_0^c(r/r_l) - \psi_0^c(r/r_{l+1})}{\psi_0^c(0)r^2}, \\ R_L(r) &= \frac{\psi_0^c(r/r_L)}{\psi_0^c(0)r^2}. \end{aligned}$$

The corresponding kernels in Fourier space are similar to those in (3.76). For example,

$$(4.20) \quad \hat{D}_l(k) = 2\pi^2 \frac{\int_0^{kr_l/c} \psi_0^c(x) dx - \int_0^{kcr_{l+1}/c} \psi_0^c(x) dx}{c_0 k},$$

with $c_0 = \int_0^1 \psi_0^c(x) dx$.

4.6. Kernel splitting using Gaussians or PSWFs in Fourier space. As just noted, it can be convenient to carry out kernel splitting in Fourier space rather than physical space, especially when the singularity of the kernel is difficult to account for in physical space, but straightforward to handle in the Fourier representation. For the constant coefficient Green's functions of classic physics, kernel splitting in Fourier space is often very convenient since \widehat{K} is typically dimension-independent when expressed as a function of $k = |\mathbf{k}|$.

We illustrate this idea by carrying out kernel splitting for the Yukawa kernel $G_Y(r)$ using PSWFs. From (A.11), the Fourier transform of the Yukawa kernel is $\hat{G}_Y(\mathbf{k}) = \frac{1}{k^2 + \lambda^2}$ in any dimension. From (4.5) and (A.7), we obtain the following kernel splitting using Gaussians in Fourier space:

$$(4.21) \quad \hat{G}_Y(k) = \frac{1}{k^2 + \lambda^2} = \hat{M}_0(k) + \sum_{l=0}^{L-1} \hat{D}_l(k) + \hat{R}_L(k), \quad L = 0, 1, \dots, L_{\max},$$

with

$$(4.22) \quad \begin{aligned} \hat{M}_0(k) &= \frac{e^{-(k^2 + \lambda^2)\sigma_0^2/4}}{k^2 + \lambda^2}, \\ \hat{D}_l(k) &= \frac{e^{-(k^2 + \lambda^2)\sigma_{l+1}^2/4} - e^{-(k^2 + \lambda^2)\sigma_l^2/4}}{k^2 + \lambda^2}, \\ \hat{R}_L(k) &= \frac{1 - e^{-(k^2 + \lambda^2)\sigma_L^2/4}}{k^2 + \lambda^2}. \end{aligned}$$

where the σ_l are defined in (3.28). The fact that the difference and residual kernels are compactly supported to precision ϵ follows from the observation that the Fourier transforms of the difference and residual kernels can be extended to entire functions of the complexified argument k and the duality of the Fourier transform [71, Theorem 1 on pp. 30].

Using PSWFs instead, we have

$$(4.23) \quad \hat{G}_Y(k) = \frac{1}{k^2 + \lambda^2} = \hat{M}_0^c(k) + \sum_{l=0}^{L-1} \hat{D}_l^c(k) + \hat{R}_L^c(k), \quad L = 0, 1, \dots, L_{\max},$$

with

$$(4.24) \quad \begin{aligned} \hat{M}_0^c(k) &= \frac{\psi_0^c(\sqrt{k^2 + \lambda^2}r_0/c)}{\psi_0^c(0)(k^2 + \lambda^2)}, \\ \hat{D}_l^c(k) &= \frac{\psi_0^c(\sqrt{k^2 + \lambda^2}r_{l+1}/c) - \psi_0^c(\sqrt{k^2 + \lambda^2}r_l/c)}{\psi_0^c(0)(k^2 + \lambda^2)}, \\ \hat{R}_L^c(k) &= \frac{1 - \psi_0^c(\sqrt{k^2 + \lambda^2}r_L/c) / \psi_0^c(0)}{(k^2 + \lambda^2)}. \end{aligned}$$

Since ψ_0^c is an even, entire function, the Fourier transforms of the difference and residual kernels can be extended as entire functions. Thus, these two kernels are compactly supported to precision ϵ . The kernel splitting in (4.23) is independent of dimension and works for the case $\lambda = 0$ as well. In three dimensions, the expression of $\hat{D}_l^c(k)$ in (4.24) reduces to (3.77) for the $1/r$ kernel when $\lambda = 0$. In two dimensions, it provides an efficient kernel splitting for $K_0(\lambda r)$ and $\log(r)$ using PSWFs. Note that it is not so obvious how to account for the logarithmic singularity if one tries to carry out kernel splitting in physical space directly.

4.7. Handling singularities in Fourier space. When we use either Gaussians or PSWFs for kernel splitting, it is easy to enforce rapid and controlled decay of the Fourier transform of the mollified and difference kernels. Since the difference kernels are compactly supported in physical space, they are smooth in Fourier space (by the Paley-Wiener theorem) and the trapezoidal rule is spectrally accurate. That is not the case for the mollified kernel, which may be slowly decaying. In the nonoscillatory case, this leads to a singularity at the origin. In the case of the Yukawa kernel, one might expect that the exponential decay leads to the same result - and rapid convergence using the trapezoidal rule. Even though both $\hat{M}_0^c(k)$ and $\hat{R}_L^c(k)$ in (4.24) are formally smooth, however, they are nearly singular at the origin when λ is small. The same issue arises with the residual kernel as well, noting that $\hat{R}_L^c(k)$ is simply the difference between the Fourier transform of the original kernel and that of the mollified kernel at level L . Thus, as discussed in the setting of the $1/r$ kernel, it is convenient to construct a *windowed* kernel which matches the mollified kernel over the domain of interest but is rapidly attenuated to zero so that a smooth quadrature can be applied in Fourier space.

We have done this explicitly for the Laplace kernel in three dimensions in [subsection 3.1](#), where the Fourier transform (3.9) of the windowed kernel is simply the product of a Gaussian and the Fourier transform of the truncated $1/r$ kernel. The approach used there works for all kernel splittings we have discussed so far. To see this, suppose that the Fourier transform of the original kernel is $\hat{K}(k)$, and that the Fourier transform of the mollified kernel is $\hat{G}_l(k)\hat{K}(k)$, where the corresponding

function $G_l(r)$ in physical space is compactly supported to precision ϵ in a ball of radius r_l . Let the windowed kernel be defined by

$$(4.25) \quad \widehat{W}_l(k) = \widehat{G}_l(k)\widehat{T}(k),$$

where

$$(4.26) \quad \widehat{T}(k) = \int_{\mathbb{R}^d} e^{-i\mathbf{k}\cdot\mathbf{x}} K(\mathbf{x}) \chi\left(\frac{|\mathbf{x}|}{(1+\sqrt{d})r_l}\right) d\mathbf{x} = \int_{|\mathbf{x}|\leq(1+\sqrt{d})r_l} e^{-i\mathbf{k}\cdot\mathbf{x}} K(\mathbf{x}) d\mathbf{x}.$$

Here, $\chi(r) = 1$ for $0 \leq r \leq 1$, $\chi(r) = 0$ for $r > 1$, and thus, $\widehat{T}(k)$ is simply the Fourier transform of the truncated kernel introduced in in [74]. Then

$$(4.27) \quad W_l(r) = M_l(r), \quad r \leq \sqrt{d}r_l.$$

In order to show this, we make use of the convolution theorem:

$$(4.28) \quad \begin{aligned} M_l(\mathbf{x}) &= \int_{\mathbb{R}^d} K(\mathbf{y})G_l(\mathbf{x} - \mathbf{y})d\mathbf{y} \\ &= \int_{|\mathbf{y}|\leq(1+\sqrt{d})r_l} K(\mathbf{y})G_l(\mathbf{x} - \mathbf{y})d\mathbf{y}, \end{aligned}$$

where we have used the fact that $G_l(\mathbf{x} - \mathbf{y}) = 0$ for \mathbf{y} outside the ball of radius $(1 + \sqrt{d})r_l$ when $|\mathbf{x}| \leq \sqrt{d}r_l$, since $G_l(r)$ is compactly supported in a ball of radius r_l to the desired precision. Likewise,

$$(4.29) \quad \begin{aligned} W_l(\mathbf{x}) &= \int_{\mathbb{R}^d} T(\mathbf{y})G_l(\mathbf{x} - \mathbf{y})d\mathbf{y} \\ &= \int_{\mathbb{R}^d} K(\mathbf{y})\chi(|\mathbf{y}|/(1+\sqrt{d})r_l)G_l(\mathbf{x} - \mathbf{y})d\mathbf{y} \\ &= \int_{|\mathbf{y}|\leq(1+\sqrt{d})r_l} K(\mathbf{y})G_l(\mathbf{x} - \mathbf{y})d\mathbf{x}. \end{aligned}$$

Since $W_l(r) = M_l(r)$ over the range of interest but compactly supported, simple trapezoidal quadrature can be applied in Fourier space with spectral accuracy.

5. Numerical results. We have implemented the algorithms described above in Fortran. The software was compiled using the Intel compiler and linked with the Intel MKL library, with all experiments run in single-threaded mode on a 3.30GHz Intel(R) Xeon(R) Gold 6234 CPU. We first consider the DMK approach in the discrete setting, for (1.1).

5.1. The ‘‘point code’’: fast transforms using the discrete DMK framework. We begin with the Laplace kernel $1/r$ in three dimensions, since it is such a well-studied problem, and there are numerous open source libraries for this task, including the FMM3D and PVFMM libraries.

5.1.1. The 3D Laplace kernel. In our implementation, we set the subdivision parameter n_s (the maximum number of points in a leaf node) to 280 for precisions $\epsilon = 10^{-3}, 10^{-6}$ and to 800 for $\epsilon = 10^{-9}, 10^{-12}$. For the PVFMM, the multipole expansion order is set to 4, 7, 11, 15 for $\epsilon = 10^{-3}, 10^{-6}, 10^{-9}, 10^{-12}$, respectively. Figure 5.1 shows the total time in seconds when the points are uniformly distributed in the unit box with the number of points $N = m \cdot 10^6$ for $m = 1, \dots, 8$, and Figure 5.2 shows

the total time in second when the points are distributed on a sphere of radius 0.45 centered at the origin. For low accuracy ($\epsilon = 10^{-3}$), the time for building the tree and sorting the points to create the adaptive data structure takes roughly one-third of the total time.

In [Figure 5.3](#), we show the average throughput of these schemes. Note that the DMK performance is very close to that of the PVFMM, while FMM3D is slower by a modest factor. We conjecture that for the $1/r$ kernel, a fully optimized scheme that uses features from each of FMM3D, PVFMM and DMK may be able to do significantly better.

REMARK 5.1. For direct interactions (as in PVFMM and FMM3D), we make use of SIMD accelerated kernel evaluation for $1/r$ (on a single core), using the Scientific computing template library (SCTL) [54].

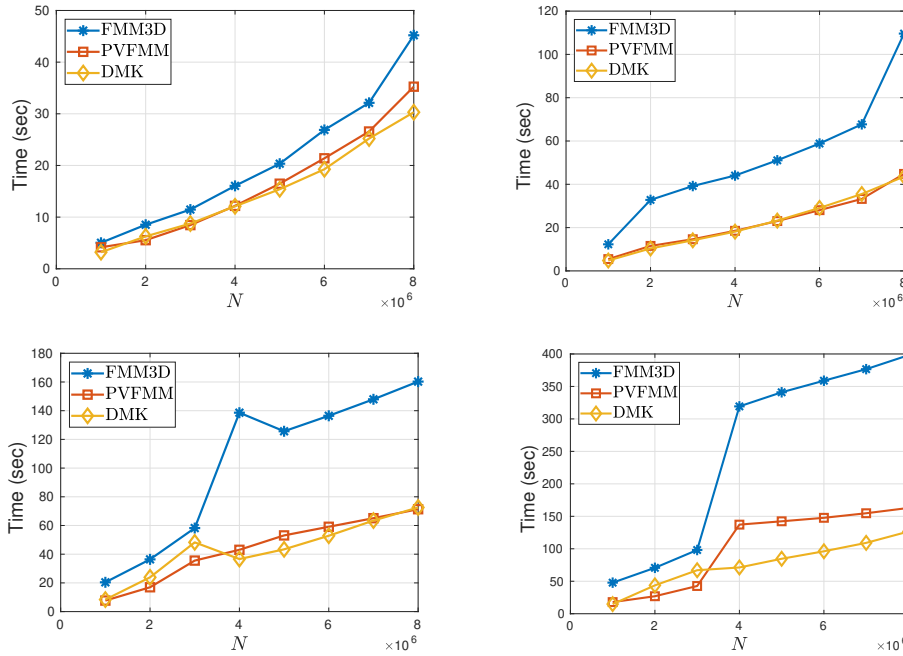


Fig. 5.1: Linear scaling of DMK for the 3D Laplace kernel and comparison with the FMM3D and PVFMM libraries for various precisions ϵ . In these figures, the points are uniformly distributed in the unit box. The x -axis indicates the total number of points and the y -axis the total time in seconds. Top left: $\epsilon = 10^{-3}$; top right: $\epsilon = 10^{-6}$. Bottom left: $\epsilon = 10^{-9}$; bottom right: $\epsilon = 10^{-12}$.

5.1.2. The 3D kernels for the square-root of the Laplacian and the Yukawa operator. In three dimensions, the kernel for the square-root of the Laplacian is $1/r^2$ and for the Yukawa operator is $e^{-\lambda r}/r$. Since SIMD-accelerated evaluation for $1/r^2$ is straightforward, we set n_s to have the same value as for the Laplace kernel. Since the Yukawa kernel is not scale-invariant, acceleration is more difficult, we reduce the magnitude of n_s to adjust the balance between far field and local work. We set $n_s = 40, 80, 300, 600$ for $\epsilon = 10^{-3}, 10^{-6}, 10^{-9}, 10^{-12}$, respectively. In [Figure 5.4](#), we see the linear scaling performance of DMK for these two kernels. In [Figure 5.5](#),

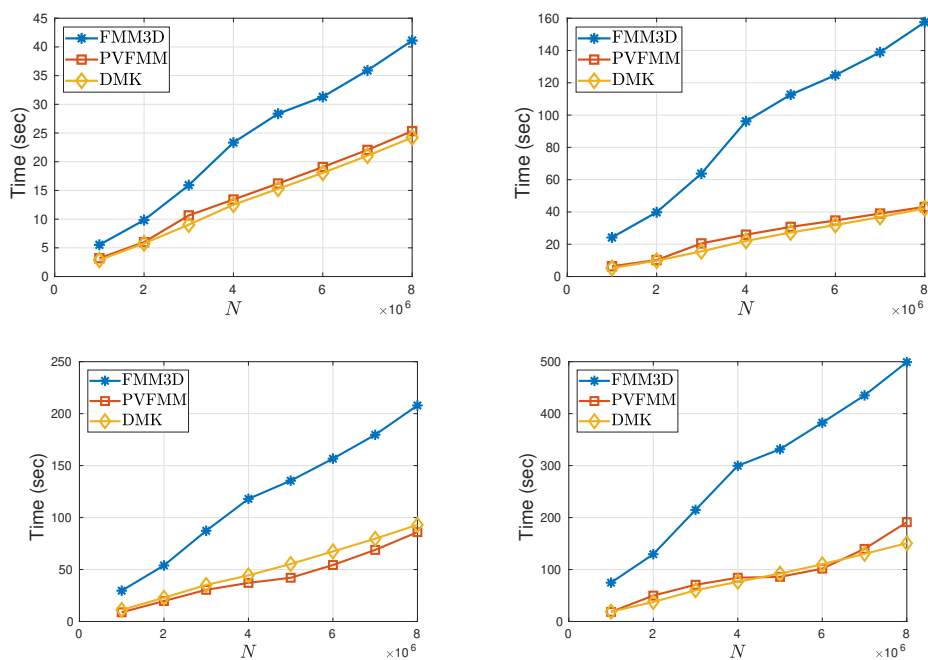


Fig. 5.2: Linear scaling of DMK for the 3D Laplace kernel and comparison with the FMM3D and PVFMM libraries for various precisions ϵ . In these figures, the points are uniformly distributed on a sphere of radius 0.45. The x -axis is the total number of points and the y -axis the total time in seconds. Top left: $\epsilon = 10^{-3}$; top right: $\epsilon = 10^{-6}$. Bottom left: $\epsilon = 10^{-9}$; bottom right: $\epsilon = 10^{-12}$.

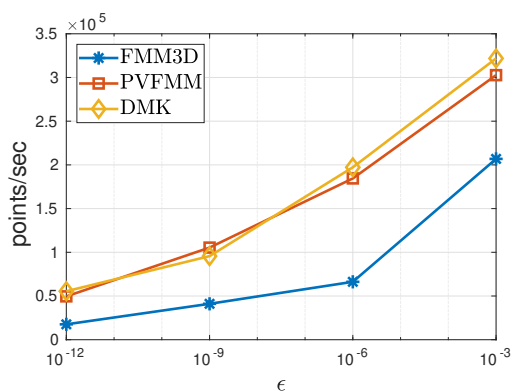


Fig. 5.3: Average throughput of DMK for the 3D Laplace kernel and comparison with the FMM3D and PVFMM libraries. The x -axis indicates the prescribed precision ϵ , and the y -axis indicates the throughput measured in 10^5 points per second.

we show the throughput in the DMK framework. Note that the throughput for the square-root of the Laplacian is similar to that for the Laplacian, while the throughput of the 3D Yukawa kernel is significantly worse - due almost entirely to the increased

expense of direct kernel evaluation.

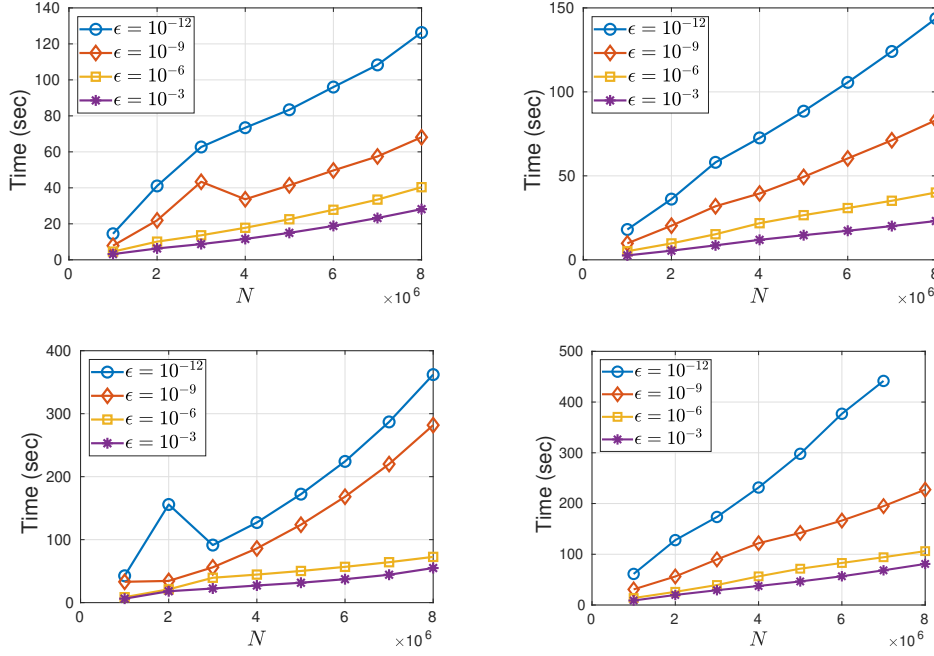


Fig. 5.4: Timing results of DMK . Top: the kernel for the square-root of the Laplacian in 3D; bottom: the kernel for the Yukawa operator in 3D with $\lambda = 6$. Left: data for uniform distribution of points; right: data points distributed on a sphere.

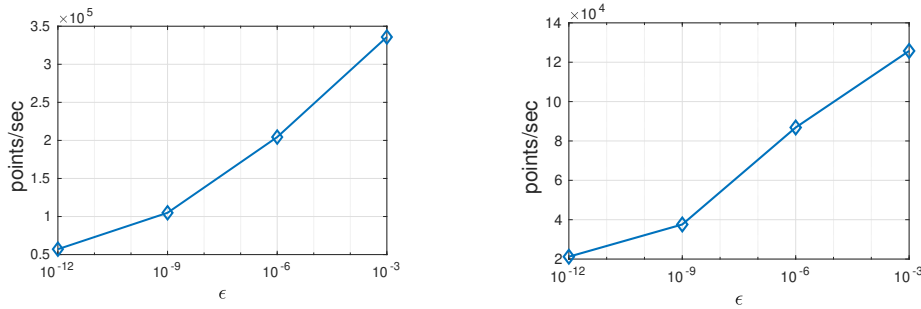


Fig. 5.5: Average throughput of DMK . Left: the kernel for the square-root of the Laplacian in 3D; right: the kernel for the Yukawa operator in 3D with $\lambda = 6$.

5.1.3. Kernels for the Laplace operator, the square-root of the Laplace operator and the Yukawa operator in 2D. In two dimensions, the kernels for Laplacian, the square-root of the Laplacian and the Yukawa operator are $\log(r)$, $1/r$, and $K_0(\lambda r)$, respectively. Both $\log(r)$ and $1/r$ are easy to rescale and admit straightforward SIMD-accelerated fast kernel evaluation. In our implementation, we set $n_s = 120, 120, 160, 160$ for $\epsilon = 10^{-3}, 10^{-6}, 10^{-9}, 10^{-12}$, respectively. Since the 2D

Table 5.1: Timing results for various stages of the DMK algorithm for the Laplace kernel, the kernel for the square-root of the Laplacian and the Yukawa kernel in two and three dimensions. The number of source points is four million on either a circle (2D) or a sphere (3D). The requested precision is $\epsilon = 10^{-6}$. n_s is the maximum number of particles in a leaf box. t_{tree} is the time for constructing the level-restricted tree from the particle distribution. t_{Fourier} is the time for translating plane-wave expansions. t_{direct} is the time for computing direct interactions using the residual kernel. t_{total} is the total computational time.

Kernel	n_s	t_{tree}	t_{Fourier}	t_{direct}	t_{total}
Two dimensions					
$\log(r)$	120	4.98	0.91	2.11	8.58
$1/r$	120	4.99	0.91	1.48	7.96
$K_0(\lambda r)$	120	5.03	0.90	22.3	28.8
$K_0(\lambda r)$	30	8.66	2.91	5.68	19.1
Three dimensions					
$1/r$	280	4.81	7.06	6.99	21.3
$1/r^2$	280	4.82	8.04	6.23	21.8
$e^{-\lambda r}/r$	280	5.33	7.17	63.4	78.3
$e^{-\lambda r}/r$	80	11.0	18.3	19.6	56.4

Yukawa kernel is not scale-invariant, we have not yet developed a SIMD-accelerated kernel routine. Thus, we set $n_s = 30, 30, 45, 45$ for $\epsilon = 10^{-3}, 10^{-6}, 10^{-9}, 10^{-12}$, respectively. In Figure 5.6, we illustrate the linear scaling of DMK for these three kernels. Figure 5.7 shows the average throughput.

REMARK 5.2. *We make use of the fast kernel evaluation routine for $\log(r)$ from the C++ vector class library [28].*

In both two and three dimensions, the principal reason the performance for the Yukawa kernel is slower than that for the Laplacian or its square root is that we lack a SIMD-accelerated direct kernel evaluation routine. In Table 5.1, we show a breakdown of the timing for various components of the algorithm. Note that the cost of translating plane-wave representations is basically the same for all kernels, so long as the tree has the same depth, and that the increase in the total time required for the Yukawa kernel is due to the ten-fold increase in the cost of kernel evaluation (t_{direct}), when n_s is set to the same number as for the other two kernels. By shrinking n_s , which cause one more level of refinement, the total cost for the Yukawa kernel is reduced slightly.

5.2. The “box code”: fast transforms using the continuous DMK framework. The performance of DMK for computing volume integrals of the form (1.2) is much less dependent on the specific kernel, once the requested precision and polynomial approximation order k for the input density are fixed. Figure 5.8 shows the average throughput of the algorithm for six kernels: the Laplace kernels in two and three dimensions ($\log(r)$ and $1/r$), the Yukawa kernels in two the three dimensions ($K_0(\lambda r)$ and $e^{-\lambda r}/r$), and the kernels for the square-root of the Laplacian in two and three dimensions ($1/r$ and $1/r^2$). In the two-dimensional setting, we fixed k to be 16.

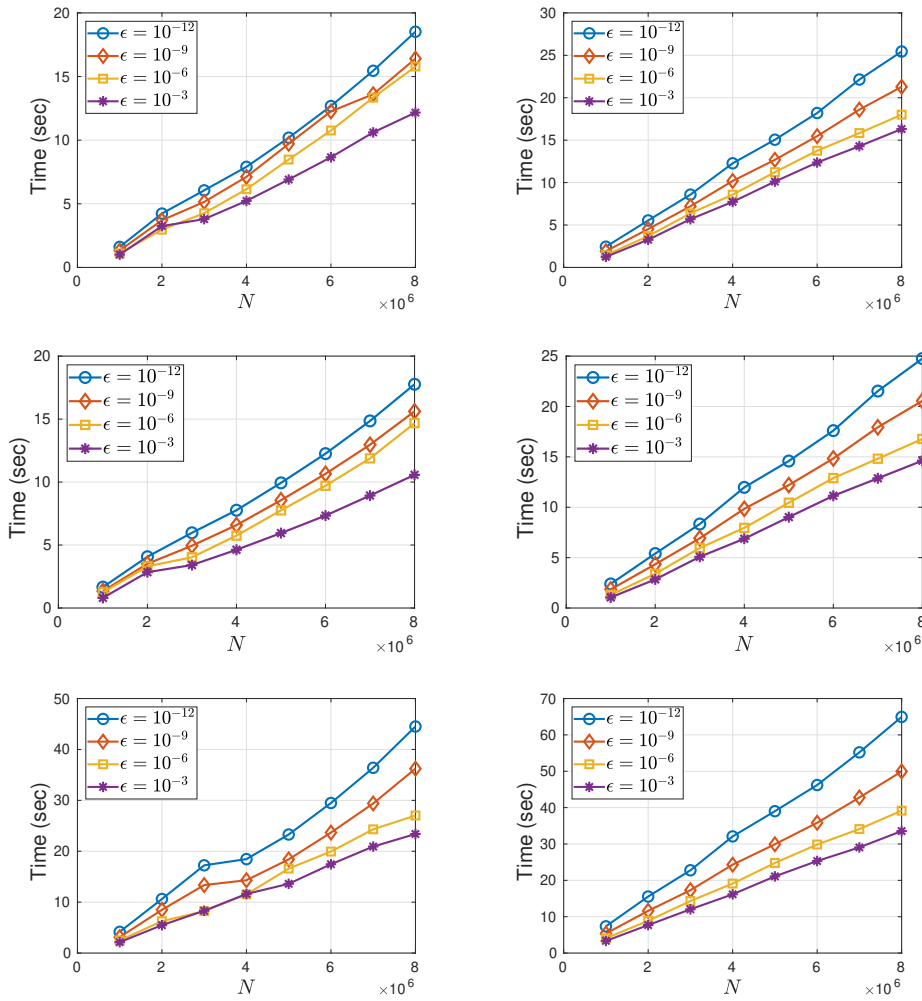


Fig. 5.6: Timing results of DMK for various 2D kernels. Top: the Laplace kernel; middle: the kernel for the square-root of the Laplacian; bottom: the Yukawa kernel with $\lambda = 6$. Left: uniform distribution; right: points distributed on a circle.

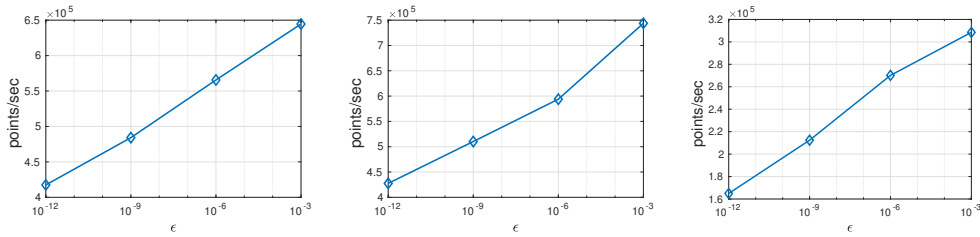


Fig. 5.7: Average throughput of DMK for 2D kernels. Left: the Laplace kernel; middle: the kernel for the square-root of the Laplacian; right: the Yukawa kernel with $\lambda = 6$.

For three dimensions, we set $k = 16$ for three and six digits of accuracy and $k = 20$ for nine and twelve digits of accuracy. The throughput of PVFMM for the 3D Laplace kernel is generated with multipole expansion orders $p = 4, 8, 12, 15$ and polynomial expansion orders $k = 6, 10, 14, 16$ for 3, 6, 9, 12 digits of accuracy, respectively.

For our experiments involving the Laplace and Yukawa kernels in three dimensions, we used an analytic solution given as the sum of two Gaussians:

$$(5.1) \quad u_{\text{exact}}(\mathbf{x}) = \frac{1}{\pi\delta^{d/2}} e^{-|\mathbf{x}-\mathbf{x}_1|^2/\delta} - \frac{1}{2\pi\delta^{d/2}} e^{-|\mathbf{x}-\mathbf{x}_2|^2/\delta}$$

with $\mathbf{x}_1 = (0.1, 0.02, 0.04)$ and $\mathbf{x}_2 = (0.03, -0.1, 0.05)$. We calculate the average throughput with $\delta = 4 \cdot 10^{-3}, 10^{-3}, 10^{-4}, 10^{-5}$. In the two-dimensional case, we used an analytic solution given by

$$(5.2) \quad u_{\text{exact}}(\mathbf{x}) = e^{-(|\mathbf{x}|/r_0)^\alpha}$$

with $r_0 = 0.25$. The solution drops sharply beyond the circle of radius r_0 (see, for example, [55, 53]). We calculate the average throughput over the parameter values $\alpha = 60, 96, 110, 180$. The input density is computed explicitly as $\rho(\mathbf{x}) = \Delta u_{\text{exact}}(\mathbf{x})$ and $\rho(\mathbf{x}) = (\Delta + \lambda^2)u_{\text{exact}}(\mathbf{x})$ for the Laplace and Yukawa kernels, respectively. The adaptive tree is constructed by querying for values of $\rho(\mathbf{x})$ until it is resolved to the desired precision.

For the kernels corresponding to the square-root of the Laplacian, the input density is assumed to be the sum of 40 Gaussians with centers at 40 equispaced points on the circle of radius 0.15 in two dimensions and variance δ . The average throughput is calculated over parameter values $\delta = 10^{-5}, 10^{-5}/3, 10^{-5}/9, 10^{-5}/27$. In three dimensions, the input density is given by (5.1). A reference solution is then calculated via the integral representation

$$(5.3) \quad \frac{1}{r^\alpha} = \frac{1}{\Gamma(\alpha/2)} \int_{-\infty}^{\infty} e^{-r^2 e^t + \alpha t/2} dt$$

and the fact that the convolution of two Gaussians is another Gaussian

$$(5.4) \quad \int_{\mathbb{R}^d} e^{-a|\mathbf{x}-\mathbf{y}|^2} e^{-b|\mathbf{y}|^2} d\mathbf{y} = \left(\frac{\pi}{a+b}\right)^{d/2} e^{-ab|\mathbf{x}|^2/(a+b)}.$$

This leads to

$$(5.5) \quad \int_{\mathbb{R}^d} \frac{e^{-|\mathbf{y}-\mathbf{y}_0|^2/\delta}}{|\mathbf{x}-\mathbf{y}|^\alpha} d\mathbf{y} = \frac{1}{\Gamma(\alpha/2)} \int_{-\infty}^{\infty} \left(\frac{\pi}{e^t + 1/\delta}\right)^{d/2} e^{-|\mathbf{x}-\mathbf{y}_0|^2/(e^{-t}+\delta) + \alpha t/2} dt.$$

Finally, (5.5) can be evaluated numerically via the truncated trapezoidal rule, since the integrand decays exponentially to zero at $\pm\infty$.

The reason that the performance of the box code has such a weak dependence on the kernel itself is that the direct interactions are accelerated by the sum-of-Gaussians approximation of the kernel as well as asymptotic analysis. Thus the cost of near-field interactions does not depend on the cost of evaluating the kernel itself. Furthermore, the cost of direct interactions goes down dramatically because of separation of variables. (It is also much more suitable for low-level code optimization across heterogeneous computer architectures.)

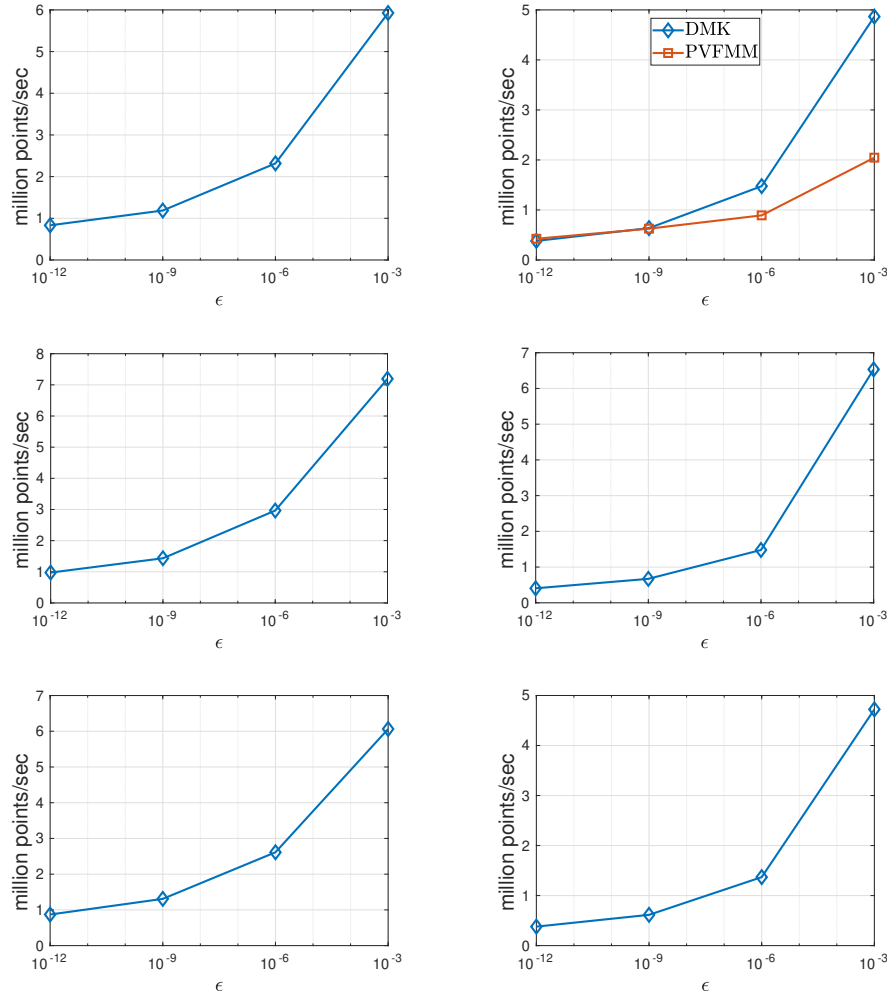


Fig. 5.8: Throughput of DMK for various kernels with continuous source distributions in two and three dimensions. The x -axis is the prescribed precision, and the y -axis is the throughput measured in million points per second. Top: the Laplace kernel; middle: the Yukawa kernel with $\lambda = 6$; bottom: the square-root Laplace kernel. Timings for 2D are on the left. Timings for 3D are on the right.

REMARK 5.3. *We have used the sum-of-Gaussians approximation in our current implementation of the box code, due to the fact that the SOG approximation is easily computed on the fly. Further speedup could be obtained if we carried out kernel-splitting using PSWFs, and used the SOG approximation only for the residual kernel. We estimate that the throughput would increase by a factor of 1.5 – 2.*

6. Conclusions. We have presented a new class of methods for the development of discrete and continuous fast transforms with translation invariant kernels. It draws from a wide variety of existing schemes: Ewald summation (which exploits Fourier analysis and diagonalization), multilevel summation (which exploits kernel splitting and hierarchical localization), and fast multipole methods (which exploit the use of

translation operators).

The DMK framework starts with a hierarchical splitting of the given kernel as a sum of windowed, difference, and residual kernels. In the execution of the method, all relevant interactions take place within a box and its nearest neighbors at every level of the grid hierarchy. This turns out to be much simpler than manipulating the “interaction lists” that are essential in the FMM to ensure the well-separateness criterion. While the rank of the far-field interaction is increased compared to the FMM, the ability to use diagonal translation via localized Fourier transforms and acceleration of near-field interactions using tensor product transforms makes the DMK framework competitive with the FMM, even for the Laplace kernel in three dimensions. More striking is the fact that the performance of DMK-based transforms is more or less independent of the kernel, so long as it is smooth away from the origin in Fourier space, especially for continuous sources. In that setting, the near neighbor interactions are computed using either tensor product transforms or asymptotics, with only one-dimensional transformation matrices needed (which can be computed on the fly). For discrete transforms, the cost is more variable, because of the need to compute near field interactions using the residual kernel. We believe that this is an area where significant improvements can be made, including better single core SIMD parallelism.

We have focused in this paper on a broad class of non-oscillatory kernels, only some of which were Green’s functions for an underlying PDE. For mildly oscillatory kernels, DMK can be applied without significant modification. In the truly high-frequency regime, however, a fast algorithm will require some additional tools: either coupling to the high-frequency FMM (as in [18, 17]) or to a butterfly factorization [41, 51, 60], or possibly by a modification of the DMK framework using adaptive quadrature in the Fourier domain, as in [8]. We considered only free-space interactions here, but it should be clear that, in the DMK framework singly, doubly or triply periodic conditions are easy to apply since they only involve modification of the Fourier representation at the root of the tree where the windowed kernel is applied (as in the fast Ewald method of [65]). In the continuous case, we have restricted ourselves to functions defined on the unit box B_0 , rather than a complex domain $\Omega \subset B_0$. Extensions to this case are being developed and will be reported at a later date.

Finally, it is worth noting that, using DMK, we represent the dense kernel matrix as the sum of matrices, which are low rank but dense at coarse levels but high-rank and sparse at finer levels. This is in contrast with the hierarchical compression of well-separated blocks of the matrix, which underlies the FMM, \mathcal{H} -matrices and skeletonization-based schemes. The latter provide a route, not just to fast transforms, but to fast matrix inversion. This suggests the investigation of DMK as an alternative route to the design of fast solvers as well.

Acknowledgments. The authors would like to thank Alex Barnett, Charles Epstein, and Manas Rachh at the Flatiron Institute for useful discussions. They would particularly like to thank Libin Lu and Dhairya Malhotra at the Flatiron Institute for their help in the implementation of the SIMD vectorization of local interactions. Finally, they would like to thank Philip Greengard at Columbia University for providing software for the evaluation of PSWFs.

REFERENCES

- [1] L. AF KLINTEBERG, D. S. SHAMSHIRGAR, AND A.-K. TORNBORG, *Fast Ewald summation for free-space Stokes potentials*, Res. Math. Sci., 4 (2017), p. 1.
- [2] T. ASKHAM, L. GREENGARD, L. LU, J. MAGLAND, D. MALHOTRA, M. O’NEAL, AND M. RACHH,

- Flatiron Institute Fast Multipole Libraries for the Laplace and Helmholtz kernels in three dimensions*. <https://github.com/flatironinstitute/FMM3D>, 2021.
- [3] J. BAGGE AND A.-K. TORNBERG, *Fast Ewald summation for Stokes flow with arbitrary periodicity*, arXiv:2210.01255, (2022).
 - [4] A. BARNETT, J. MAGLAND, AND L. AF KLINTEBERG, *A parallel non-uniform fast Fourier transform library based on an “exponential of semicircle” kernel*, SIAM J. Sci. Comput., 41 (2019), pp. C479–C504.
 - [5] A. H. BARNETT, *Aliasing error of the $\exp(\beta\sqrt{1-z^2})$ kernel in the nonuniform fast Fourier transform*, Applied and Computational Harmonic Analysis, 51 (2021), pp. 1–16.
 - [6] A. H. BARNETT *et al.*, *Non-uniform fast Fourier transform library of types 1, 2, 3 in dimensions 1, 2, 3*. <https://github.com/ahbarnett/finufft>, 2018.
 - [7] C. BERTOGLIO AND B. N. KHOROMSKIJ, *Low-rank quadrature-based tensor approximation of the Galerkin projected Newton/Yukawa kernels*, Computer Physics Communications, 183 (2012), pp. 904–912.
 - [8] G. BEYLKIN, C. KURCZ, AND L. MONZÓN, *Fast convolution with the free space Helmholtz Green’s function*, Journal of Computational Physics, 228 (2009), pp. 2770–2791.
 - [9] G. BEYLKIN AND M. J. MOHLENKAMP, *Numerical operator calculus in higher dimensions*, Proc. Natl. Acad. Sci., 16 (2002), pp. 10246–10251.
 - [10] G. BEYLKIN AND L. MONZÓN, *Approximation by exponential sums revisited*, Applied and Computational Harmonic Analysis, 28 (2010), pp. 131–149.
 - [11] J. P. BOYD, *Chebyshev and Fourier Spectral methods*, Dover, 2000.
 - [12] A. BRANDT AND A. LUBRECHT, *Multilevel matrix multiplication and fast solution of integral equations*, Journal of Computational Physics, 90 (1990), pp. 348–370.
 - [13] A. BRANDT AND C. H. VENNER, *Multilevel evaluation of integral transforms with asymptotically smooth kernels*, SIAM Journal on Scientific Computing, 19 (1998), pp. 468–492.
 - [14] J. BREMER, Z. GIMBUTAS, AND V. ROKHLIN, *A nonlinear optimization procedure for generalized Gaussian quadratures*, SIAM J. Sci. Comput., 32 (2010), pp. 1761–1788.
 - [15] J. CARRIER, L. GREENGARD, AND V. ROKHLIN, *A fast adaptive multipole algorithm for particle simulations*, SIAM J. Sci. Statist. Comput., 9 (1988), pp. 669–686.
 - [16] D. S. CERUTTI AND D. A. CASE, *Multi-level Ewald: A hybrid multigrid/fast Fourier transform approach to the electrostatic particle-mesh problem*, Journal of Chemical Theory and Computation, 6 (2010), pp. 443–458. PMID: 22039358.
 - [17] H. CHENG, W. Y. CRUTCHFIELD, Z. GIMBUTAS, L. GREENGARD, J. F. ETHRIDGE, J. HUANG, V. ROKHLIN, N. YARVIN, AND J. ZHAO, *A wideband fast multipole method for the Helmholtz equation in three dimensions*, J. Comput. Phys., 216 (2006), pp. 300–325.
 - [18] H. CHENG, W. Y. CRUTCHFIELD, Z. GIMBUTAS, J. H. L. GREENGARD, V. ROKHLIN, N. YARVIN, AND J. ZHAO, *Remarks on the implementation of the wideband FMM for the Helmholtz equation in two dimensions*, Contemp. Math., 408 (2006), pp. 99–110.
 - [19] H. CHENG, L. GREENGARD, AND V. ROKHLIN, *A fast adaptive multipole algorithm in three dimensions*, J. Comput. Phys., 155 (1999), pp. 468–498.
 - [20] H. CHENG, L. GREENGARD, AND V. ROKHLIN, *A fast adaptive multipole algorithm in three dimensions*, J. Comput. Phys., 155 (1999), pp. 468–498.
 - [21] T. DARDEN, D. YORK, AND L. PEDERSEN, *Particle mesh Ewald - an $o(n \log n)$ method for Ewald sums in large systems*, J. Chem. Phys., 98 (1993), pp. 10089–10092.
 - [22] A. DUTT AND V. ROKHLIN, *Fast Fourier transforms for nonequispaced data*, SIAM J. Sci. Comput., 14 (1993), pp. 1368–1393.
 - [23] ———, *Fast Fourier transforms for nonequispaced data. II*, Appl. Comput. Harmon. Anal., 2 (1995), pp. 85–100.
 - [24] H. DYM AND H. P. MCKEAN, *Fourier series and integrals*, vol. 14 of Probability and Mathematical Statistics, Academic Press, 1975.
 - [25] C. EPSTEIN AND S. JIANG, *A stable, efficient scheme for C^n function extensions on smooth domains in \mathbb{R}^d* , arXiv:2206.11318, (2022).
 - [26] G. ESTRIN, *Organization of computer systems: the fixed plus variable structure computer*, Proc. Western Joint Comput. Conf., (1960), pp. 33–40.
 - [27] P. P. EWALD, *Die berechnung optischer und elektrostatischer gitterpotentiale*, Annalen der physik, 369 (1921), pp. 253–287.
 - [28] A. FOG, *C++ vector class library*. <https://github.com/vectorclass/version2>, 2023.
 - [29] G. B. FOLLAND AND A. SITARAM, *The uncertainty principle: a mathematical survey*, Journal of Fourier analysis and applications, 3 (1997), pp. 207–238.
 - [30] W. FONG AND E. DARVE, *The black-box fast multipole method*, J. Comput. Phys., 228 (2009), pp. 8712–8725.
 - [31] M. FRIGO AND S. G. JOHNSON, *The fastest Fourier transform in the west*, Tech. Report MIT-

- LCS-TR-728, Massachusetts Institute of Technology, September 1997.
- [32] ———, *FFTW: An adaptive software architecture for the FFT*, in Proc. 1998 IEEE Intl. Conf. Acoustics Speech and Signal Processing, vol. 3, IEEE, 1998, pp. 1381–1384.
 - [33] Z. GAO, J. LIANG, AND Z. XU, *A kernel-independent sum-of-exponentials method*, Journal of Scientific Computing, 93 (2022), pp. 1–35.
 - [34] Z. GIMBUTAS AND V. ROKHLIN, *A generalized fast multipole method for nonoscillatory kernels*, SIAM J. Sci. Comput., 24 (2002), pp. 796–817.
 - [35] K. GLOVER, *All optimal Hankel-norm approximations of linear multivariable systems and their L^∞ -error bounds*, International Journal of Control, 39 (1984), pp. 1115–1193.
 - [36] L. GREENGARD, S. JIANG, M. RACHH, AND J. WANG, *A new version of the adaptive fast Gauss transform for discrete and continuous sources*, arXiv:2305.07165, (2023).
 - [37] L. GREENGARD, S. JIANG, AND Y. ZHANG, *The anisotropic truncated kernel method for convolution with free-space Green’s functions*, SIAM Journal on Scientific Computing, 40 (2018), pp. A3733–A3754.
 - [38] L. GREENGARD AND J. LEE, *Accelerating the nonuniform fast Fourier transform*, SIAM Rev., 46 (2004), pp. 443–454.
 - [39] L. GREENGARD AND V. ROKHLIN, *A fast algorithm for particle simulations*, J. Comput. Phys., 73 (1987), pp. 325–348.
 - [40] ———, *A new version of the fast multipole method for the Laplace equation in three dimensions*, in Acta numerica, 1997, vol. 6 of Acta Numer., Cambridge Univ. Press, 1997, pp. 229–269.
 - [41] H. GUO, Y. LIU, J. HU, AND E. MICHIELSEN, *A butterfly-based direct integral-equation solver using hierarchical lu factorization for analyzing scattering from electrically large conducting objects*, IEEE Transactions on Antennas and Propagation, 65 (2017), pp. 4742–4750.
 - [42] W. HACKBUSCH, *A sparse matrix arithmetic based on H-matrices. Part I: Introduction to H-matrices*, Computing, 62 (1999), pp. 89–108.
 - [43] W. HACKBUSCH AND S. BÖRM, *Data-sparse approximation by adaptive H^2 -matrices*, Computing, 69 (2002), pp. 1–35.
 - [44] D. J. HARDY, J. E. STONE, AND K. SCHULTEN, *Multilevel summation of electrostatic potentials using graphics processing units*, Parallel computing, 35 (2009), pp. 164–177.
 - [45] D. J. HARDY, Z. WU, J. C. PHILLIPS, J. E. STONE, R. D. SKEEL, AND K. SCHULTEN, *Multilevel summation method for electrostatic force evaluation*, Journal of Chemical Theory and Computation, 11 (2015), pp. 766–779. PMID: 25691833.
 - [46] R. HARRISON, G. FANN, T. YANAI, Z. GAN, AND G. BEYLKIN, *Multiresolution quantum chemistry: basic theory and initial applications*, J. Chem. Phys., 121 (2004), pp. 11587–11598.
 - [47] N. J. HIGHAM, *Stability analysis of algorithms for solving confluent Vandermonde-like systems*, SIAM J. Matrix Anal. Appl., 11 (1990), pp. 23–41.
 - [48] K. L. HO AND L. GREENGARD, *A fast direct solver for structured linear systems by recursive skeletonization*, SIAM Journal on Scientific Computing, 34 (2012), pp. 2507–2532.
 - [49] R. HOCKNEY AND J. EASTWOOD, *Computer Simulation Using Particles*, McGraw-Hill, NY, 1981.
 - [50] H. KAYA, D. J. HARDY, AND R. D. SKEEL, *Multilevel summation for periodic electrostatics using B-splines*, The Journal of Chemical Physics, 154 (2021). 144105.
 - [51] Y. LI, H. YANG, E. MARTIN, K. L. HO, AND L. YING, *Butterfly factorization*, Multiscale Model. Simul., 13 (2015), pp. 714–732.
 - [52] J. MA, V. ROKHLIN, AND S. WANDZURA, *Generalized Gaussian quadrature rules for systems of arbitrary functions*, SIAM J. Numer. Anal., 33 (1996), pp. 971–996.
 - [53] D. MALHOTRA, *A parallel kernel-independent fmm library for particle and volume potentials*. <https://github.com/dmalhotra/pvfmm>, 2015.
 - [54] D. MALHOTRA, *Scientific computing template library*. <https://github.com/dmalhotra/SCTL>, 2022.
 - [55] D. MALHOTRA AND G. BIROS, *PVFMM: a parallel kernel independent FMM for particle and volume potentials*, Commun. Comput. Phys., 18 (2015), pp. 808–830.
 - [56] V. MINDEN, K. L. HO, A. DAMLE, AND L. YING, *A recursive skeletonization factorization based on strong admissibility*, Multiscale Model. Simul., 15 (2017), pp. 768–796.
 - [57] G. MORIMOTO, Y. M. KOYAMA, H. ZHANG, T. S. KOMATSU, Y. OHNO, K. NISHIDA, I. OHMURA, H. KOYAMA, AND M. TAJI, *Hardware acceleration of tensor-structured multilevel Ewald summation method on MDGRAPE-4A, a special-purpose computer system for molecular dynamics simulations*, in Proceedings of the International Conference for High Performance Computing, Networking, Storage and Analysis, SC ’21, New York, NY, USA, 2021, Association for Computing Machinery.
 - [58] K. NABORS, F. T. KORSMEYER, F. T. LEIGHTON, AND J. WHITE, *Preconditioned, adaptive, multipole-accelerated iterative methods for three-dimensional first-kind integral equations*

- of potential theory, SIAM J. Sci. Statist. Comput., 15 (1994), p. 714.
- [59] F. W. J. OLVER, D. W. LOZIER, R. F. BOISVERT, AND C. W. CLARK, eds., *NIST Handbook of Mathematical Functions*, Cambridge University Press, May 2010.
- [60] M. O'NEIL, F. WOOLFE, AND V. ROKHLIN, *An algorithm for the rapid evaluation of special function transforms*, Appl. Comput. Harm. Anal., 28 (2010), pp. 203–226.
- [61] A. OSIPOV, V. ROKHLIN, AND H. XIAO, *Prolate spheroidal wave functions of order zero*, vol. 187 of Springer Ser. Appl. Math. Sci, Springer, 2013.
- [62] D. POTTS, G. STEIDL, AND A. NIESLONY, *Fast convolution with radial kernels at nonequispaced knots*, Numer. Math., 98 (2004), pp. 329–351.
- [63] M. J. D. POWELL, *Approximation theory and methods*, Cambridge university press, 1981.
- [64] V. ROKHLIN, *Rapid solution of integral equations of classical potential theory*, Journal of computational physics, 60 (1985), pp. 187–207.
- [65] D. S. SHAMSHIRGAR, J. BAGGE, AND A.-K. TORNERG, *Fast Ewald summation for electrostatic potentials with arbitrary periodicity*, The Journal of Chemical Physics, 154 (2021), p. 164109.
- [66] Y. SHAN, J. L. KLEPEIS, M. P. EASTWOOD, R. O. DROR, AND D. E. SHAW, *Gaussian split Ewald: A fast Ewald mesh method for molecular simulation*, The Journal of Chemical Physics, 122 (2005), p. 054101.
- [67] R. D. SKEEL, I. TEZCAN, AND D. J. HARDY, *Multiple grid methods for classical molecular dynamics*, Journal of Computational chemistry, 23 (2002), pp. 673–684.
- [68] E. M. STEIN AND G. WEISS, *Introduction to Fourier analysis on Euclidean spaces*, vol. 1, Princeton university press, 1971.
- [69] H. SUNDAR, R. S. SAMPATH, AND G. BIROS, *Bottom-up construction and 2 : 1 balance refinement of linear octrees in parallel*, SIAM J. Sci. Comput., 30 (2008), pp. 2675–2708.
- [70] A. Y. TOUKMAJI AND J. A. BOARD, *Ewald summation techniques in perspective: a survey*, Computer Physics Communications, 95 (1996), pp. 73–92.
- [71] L. N. TREFETHEN, *Spectral methods in MATLAB*, SIAM, 2000.
- [72] L. N. TREFETHEN, *Approximation Theory and Approximation Practice, Extended Edition*, Society for Industrial and Applied Mathematics, Philadelphia, PA, 2019.
- [73] L. N. TREFETHEN AND J. A. C. WEIDEMAN, *The exponentially convergent trapezoidal rule*, SIAM review, 56 (2014), pp. 385–458.
- [74] F. VICO, L. GREENGARD, AND M. FERRANDO, *Fast convolution with free-space Green's functions*, Journal of Computational Physics, 323 (2016), pp. 191–203.
- [75] K. XU AND S. JIANG, *A bootstrap method for sum-of-poles approximations*, J. Sci. Comput., 55 (2013), pp. 16–39.
- [76] N. YARVIN AND V. ROKHLIN, *Generalized Gaussian quadratures and singular value decompositions of integral operators*, SIAM J. Sci. Comput., 20 (1998), pp. 699–718.
- [77] L. YING, G. BIROS, AND D. ZORIN, *A kernel-independent adaptive fast multipole algorithm in two and three dimensions*, J. Comput. Phys., 196 (2004), pp. 591–626.
- [78] B. ZHANG, J. HUANG, N. P. PITSIANIS, AND X. SUN, *A Fourier-series-based kernel-independent fast multipole method*, J. Comput. Phys., 230 (2011), pp. 5807–5821.

Appendix A. Mathematical tools.

A.1. Hankel transform. The Hankel transform is defined by the formula

$$(A.1) \quad \hat{f}_\nu(k) = \int_0^\infty J_\nu(kr) f(r) r dr,$$

where

$$(A.2) \quad J_\nu(x) = \frac{\left(\frac{1}{2}x\right)^\nu}{\pi^{\frac{1}{2}}\Gamma\left(\nu + \frac{1}{2}\right)} \int_0^\pi \cos(x \cos \theta) (\sin \theta)^{2\nu} d\theta$$

is the Bessel function of the first kind of order ν [59, §10.9.4]. In particular,

$$(A.3) \quad J_0(x) = \frac{1}{\pi} \int_0^\pi e^{ix \cos \theta} d\theta, \quad J_{\frac{1}{2}}(x) = \sqrt{\frac{2x}{\pi}} \frac{\sin(x)}{x}.$$

A.2. Radially symmetric functions. Suppose that f is radially symmetric, i.e., $f(\mathbf{x}) = f(r)$. Then its Fourier transform \hat{f} is also radially symmetric. Indeed, we

have

$$(A.4) \quad k^{\frac{d-2}{2}} \hat{f}(k) = (2\pi)^{\frac{d}{2}} \int_0^\infty J_{\frac{d-2}{2}}(kr) r^{\frac{d-2}{2}} f(r) r dr.$$

That is, the Fourier transform of a radially symmetric function in \mathbb{R}^d can be computed via the Hankel transform along the radial direction. In two dimensions,

$$(A.5) \quad \hat{f}(k) = 2\pi \int_0^\infty J_0(kr) f(r) r dr.$$

In three dimensions,

$$(A.6) \quad \hat{f}(k) = 4\pi \int_0^\infty \frac{\sin(kr)}{kr} f(r) r^2 dr.$$

Some relevant Fourier transform pairs are listed below.

(a) Gaussian in \mathbb{R}^d .

$$(A.7) \quad G(\mathbf{x}) = e^{-\delta^2 r^2}, \quad \hat{G}(\mathbf{k}) = \left(\frac{\sqrt{\pi}}{\delta} \right)^d e^{-k^2/(4\delta^2)}.$$

(b) Power function in \mathbb{R}^d .

$$(A.8) \quad f(\mathbf{x}) = \frac{1}{r^\alpha}, \quad \hat{f}(\mathbf{k}) = (2\pi)^{\frac{d}{2}} \frac{2^{\frac{d-\alpha}{2}} \Gamma\left(\frac{d-\alpha}{2}\right)}{2^{\frac{\alpha}{2}} \Gamma\left(\frac{\alpha}{2}\right)} \frac{1}{k^{d-\alpha}}.$$

(c) Green's function for the Laplace operator $(-\Delta)$:

$$(A.9) \quad \begin{aligned} G_L(\mathbf{x}) &= -\frac{1}{2\pi} \log r, & \hat{G}_L(\mathbf{k}) &= \frac{1}{k^2}, & \mathbf{x} \in \mathbb{R}^2, \\ G_L(\mathbf{x}) &= \frac{1}{4\pi} \frac{1}{r}, & \hat{G}_L(\mathbf{k}) &= \frac{1}{k^2}, & \mathbf{x} \in \mathbb{R}^3. \end{aligned}$$

(d) Green's function for the Helmholtz operator $(-\Delta - \omega^2)$:

$$(A.10) \quad \begin{aligned} G_H(\mathbf{x}) &= \frac{i}{4} H_0^{(1)}(\omega r), & \hat{G}_H(\mathbf{k}) &= \frac{1}{k^2 - \omega^2}, & \mathbf{x} \in \mathbb{R}^2, \\ G_H(\mathbf{x}) &= \frac{1}{4\pi} \frac{e^{i\omega r}}{r}, & \hat{G}_H(\mathbf{k}) &= \frac{1}{k^2 - \omega^2}, & \mathbf{x} \in \mathbb{R}^3. \end{aligned}$$

Here $H_0^{(1)}$ is the Hankel function of the first kind of order zero.

(e) Green's function for the Yukawa operator $(-\Delta + \lambda^2)$:

$$(A.11) \quad \begin{aligned} G_Y(\mathbf{x}) &= \frac{1}{2\pi} K_0(\lambda r), & \hat{G}_Y(\mathbf{k}) &= \frac{1}{k^2 + \lambda^2}, & \mathbf{x} \in \mathbb{R}^2, \\ G_Y(\mathbf{x}) &= \frac{1}{4\pi} \frac{e^{-\lambda r}}{r}, & \hat{G}_Y(\mathbf{k}) &= \frac{1}{k^2 + \lambda^2}, & \mathbf{x} \in \mathbb{R}^3. \end{aligned}$$

Here K_0 is the modified Bessel function of the second kind of order zero.

A.3. Fourier transform of radially symmetric functions in three dimensions. Consider

$$(A.12) \quad F(\mathbf{x}) = \frac{\int_0^r f(u)du}{r}, \quad \mathbf{x} \in \mathbb{R}^3,$$

where f is an even nonnegative function. We also assume that

$$(A.13) \quad \lim_{r \rightarrow \infty} \int_0^r f(u)du = 0,$$

which is true for either the difference kernel or the truncated mollified kernel discussed above. Then its Fourier transform \widehat{F} can be calculated using spherical coordinates:

$$(A.14) \quad \begin{aligned} \widehat{F}(k) &= \int_0^\infty \int_0^\pi \int_0^{2\pi} e^{-i|k|r \cos \theta} F(r) r^2 \sin \theta dr d\theta d\phi \\ &= 2\pi \int_0^\infty \int_0^\pi e^{-i|k|r \cos \theta} F(r) r^2 \sin \theta dr d\theta \\ &= \frac{2\pi}{i|k|} \int_0^\infty \left(e^{i|k|r} - e^{-i|k|r} \right) F(r) r dr \\ &= \frac{2\pi}{i|k|} \int_0^\infty \left(e^{i|k|r} - e^{-i|k|r} \right) \left(\int_0^r f(u)du \right) dr \\ &= \frac{2\pi}{|k|^2} \int_0^\infty \left(e^{i|k|r} + e^{-i|k|r} \right) f(r) dr \\ &= \frac{2\pi \widehat{f}(k)}{k^2}, \end{aligned}$$

where the first equality uses the expression of the Fourier transform in spherical coordinates, the fifth equality follows from integration by parts, and the last equality follows from the assumption that f is even.

A.4. Integral representations of kernels. A unified approach to developing a telescoping sum for the kernel of interest is to begin with an integral representation in terms of exponential functions or Gaussians. Many kernels are equipped with such classical representations, suitable for the DMK framework. Some are listed below.

(a) The power function (A.8) in \mathbb{R}^d [10].

$$(A.15) \quad \begin{aligned} \frac{1}{r^\alpha} &= \frac{1}{\Gamma(\alpha)} \int_0^\infty e^{-rt} t^{\alpha-1} dt, \\ &= \frac{1}{\Gamma(\alpha/2)} \int_0^\infty e^{-r^2 t} t^{\alpha/2-1} dt, \\ &= \frac{2}{\Gamma(\alpha/2)} \int_0^\infty e^{-r^2 t^2} t^{\alpha-1} dt. \end{aligned}$$

(b) Green's function for the Laplace operator (A.9):

$$(A.16) \quad \begin{aligned} -\frac{1}{2\pi} \log r &= \frac{1}{4\pi} \int_0^\infty \frac{1}{t} e^{-r^2/(4t)} dt = \frac{1}{2\pi} \int_0^\infty e^{-r^2 t^2} \frac{dt}{t}, \\ \frac{1}{4\pi r} &= \frac{1}{8\pi^{3/2}} \int_0^\infty \frac{1}{t^{3/2}} e^{-r^2/(4t)} dt = \frac{1}{2\pi^{3/2}} \int_0^\infty e^{-r^2 t^2} dt. \end{aligned}$$

Some of these formulas must be interpreted in a distributional sense. The first expression in each line can be understood to describe the connection between the Laplace kernel and the heat kernel, viewing the solution to the Poisson equation as the solution to the initial value problem for the heat equation with the same forcing term, as the solution to the heat flow problem reaches its equilibrium state as $t \rightarrow \infty$.

(c) Green's function for the Yukawa operator (A.11), (see [7, 37]):

$$(A.17) \quad \begin{aligned} \frac{1}{2\pi} K_0(\lambda r) &= \frac{1}{2\pi} \int_0^\infty e^{-r^2 t^2 - \frac{\lambda^2}{4t^2}} \frac{dt}{t}, \quad \mathbf{x} \in \mathbb{R}^2, \\ \frac{1}{4\pi} \frac{e^{-\lambda r}}{r} &= \frac{1}{2\pi^{3/2}} \int_0^\infty e^{-r^2 t^2 - \frac{\lambda^2}{4t^2}} dt, \quad \mathbf{x} \in \mathbb{R}^3. \end{aligned}$$

(d) Green's function for the Helmholtz operator (A.10), (see [8]):

$$(A.18) \quad \begin{aligned} \frac{i}{4} H_0^{(1)}((\kappa + i\lambda)r) &= \frac{1}{2\pi} \int_0^\infty e^{-r^2 t^2 + \frac{(\kappa + i\lambda)^2}{4t^2}} \frac{dt}{t}, \quad \mathbf{x} \in \mathbb{R}^2, \\ \frac{1}{4\pi} \frac{e^{i(\kappa + i\lambda)r}}{r} &= \frac{1}{2\pi^{3/2}} \int_0^\infty e^{-r^2 t^2 + \frac{(\kappa + i\lambda)^2}{4t^2}} dt, \quad \mathbf{x} \in \mathbb{R}^3. \end{aligned}$$

(e) Inverse multiquadric:

$$(A.19) \quad \frac{1}{\sqrt{r^2 + a^2}} = \frac{2}{\sqrt{\pi}} \int_0^\infty e^{-(r^2 + a^2)t^2} dt.$$

(f) Inverse quadratic:

$$(A.20) \quad \frac{1}{r^2 + a^2} = \int_0^\infty e^{-(r^2 + a^2)t} dt.$$

A.5. Prolate spheroidal wave functions of order zero. Suppose that $c > 0$ is a real number. Prolate spheroidal wave functions (PSWFs) of order zero are eigenfunctions of the integral operator $F_c : L^2[-1, 1] \rightarrow L^2[-1, 1]$, defined by the formula

$$(A.21) \quad F_c[\phi](x) = \int_{-1}^1 \phi(t) e^{icxt} dt.$$

It is known [61] that the eigenfunctions $\psi_0^c, \psi_1^c, \dots$ of F_c are purely real, orthonormal, and complete in $L^2[-1, 1]$. The even-numbered functions are even; the odd-numbered ones are odd. Each function ψ_n has exactly n simple roots in $(-1, 1)$. All eigenvalues λ_n of F_c are nonzero and simple; the even-numbered ones are purely real, and the odd-numbered ones are purely imaginary; in particular, $\lambda_n = i^n |\lambda_n|$, for every integer $n \geq 0$.

The PSWFs provide a natural tool for the study of band-limited functions on an interval. Indeed, a function $f : \mathbb{R} \rightarrow \mathbb{C}$ is band-limited with band limit c if for all real x ,

$$(A.22) \quad f(x) = \int_{-1}^1 \sigma(t) e^{icxt} dt,$$

for some $\sigma \in L^2[-1, 1]$. It is known that if

$$(A.23) \quad \int_{-1}^1 |\sigma(t)|^2 dt = 1,$$

then

$$(A.24) \quad \int_{-1}^1 |f(x)|^2 dx \leq |\lambda_0(c)|^2.$$

The equality in (A.24) occurs only if $\sigma = \psi_0^c$.

A.6. Window functions. Window functions are widely used in signal processing and numerical analysis. In this paper, we focus on two window functions - the Gaussian (A.7) and the PSWF of order zero ψ_0^c . The Gaussian window function has a number of compelling properties. First, it appear naturally in the integral representations of many other kernels (as seen above). Second, Gaussian and its Fourier transform are both smooth and have explicit expressions via elementary functions. Third, Gaussians are the only class of functions whose d -dimensional version is simply the tensor product of its one-dimensional version. That is, if $f(\mathbf{x}) = \prod_{i=1}^d f(x_i)$ for $\mathbf{x} \in \mathbb{R}^d$ with $d \geq 2$, then $f(\mathbf{x}) = e^{-|\mathbf{x}|^2/\sigma}$ for some σ . Fourth, Gaussians satisfy several optimality properties, including minimizing the Heisenberg uncertainty for L^2 functions (the product of the second moment of f and the second moment of \hat{f} divide by the product $\|f\|_2 \|\hat{f}\|_2$) [24, 29]. While they work extremely well as window functions in finite precision (ignoring exponentially small tails), they are well-known to be sub-optimal in terms of computational efficiency. In particular, the Heisenberg property does not imply that a Gaussian is an optimal window for band-limited functions. For that, the best choice, in some sense, is the PSWF of order zero ψ_0^c . Indeed, as shown in (A.24), ψ_0^c is the function with support in $[-1, 1]$ with minimal L^2 -norm (energy) outside the frequency interval $[-c, c]$. Moreover, if we truncate ψ_0^c at $\pm c$ and its Fourier transform at $\pm c$, then

$$(A.25) \quad \hat{\psi}_0^c(k) = \lambda_0 \psi_0^c(k/c),$$

where λ_0 is the associated eigenvalue of the operator defined in (A.21). Thus, the truncated ψ_0^c is the analog of the Gaussian on a finite interval in the sense that the Fourier transform is the original function up to suitable scaling.

REMARK A.1. *It has been observed that the Kaiser-Bessel function and the “exponential of semicircle” (ES) function are very close to ψ_0^c in terms of the Fourier expansion length [5], and hence in terms of efficiency of approximation. The Kaiser-Bessel function and the ES function have the advantage of having a closed form expression, which is not the case for ψ_0^c . However, the evaluation of all such special functions can be accelerated through the use of piecewise polynomial approximation, after which the PSWF is as easy to evaluate as any other window function. In practice, we have found that the PSWF is slightly better than the Kaiser-Bessel or ES kernels in terms of the discretized Fourier expansion length, especially when the required accuracy is not very high. Thus, we use either the Gaussian or the PSWF as window functions in our numerical experiments.*